(12) INTERNATIONAL APPLICATION PUBLISHED UNDER THE PATENT COOPERATION TREATY (PCT)

(19) World Intellectual Property Organization
International Bureau

(43) International Publication Date
14 June 2018 (14.06.2018)

WIPO | PCT

(10) International Publication Number
WO 2018/106828 A1

(51) International Patent Classification:
G01R 33/44 (2006.01) *G01N 15/08* (2006.01)
G01N 23/00 (2006.01) *G01N 24/00* (2006.01)

(21) International Application Number:
PCT/US2017/064948

(22) International Filing Date:
06 December 2017 (06.12.2017)

(25) Filing Language: English

(26) Publication Language: English

(30) Priority Data:
62/431,075 07 December 2016 (07.12.2016) US

(71) Applicant: **NEW YORK UNIVERSITY** [US/US]; 70 Washington Square South, New York, New York 10012 (US).

(72) Inventors: **JERSCHOW, Alexej**; 4 Washington Square Village 5R, New York, New York 10012 (US). **ILOTT, Andrew J.**; 1310 Danchetz Court, Rahway, New Jersey 07065 (US).

(74) Agent: **MARTIN, Matthew E.** et al.; FOLEY & LARDNER LLP, 3000 K Street N.W., Suite 600, Washington, District of Columbia 20007 (US).

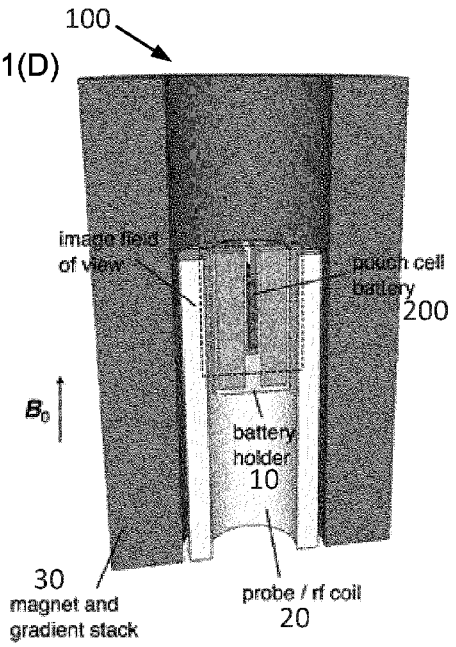
(81) Designated States *(unless otherwise indicated, for every kind of national protection available)*: AE, AG, AL, AM, AO, AT, AU, AZ, BA, BB, BG, BH, BN, BR, BW, BY, BZ, CA, CH, CL, CN, CO, CR, CU, CZ, DE, DJ, DK, DM, DO, DZ, EC, EE, EG, ES, FI, GB, GD, GE, GH, GM, GT, HN, HR, HU, ID, IL, IN, IR, IS, JO, JP, KE, KG, KH, KN, KP, KR, KW, KZ, LA, LC, LK, LR, LS, LU, LY, MA, MD, ME, MG, MK, MN, MW, MX, MY, MZ, NA, NG, NI, NO, NZ, OM, PA, PE, PG, PH, PL, PT, QA, RO, RS, RU, RW, SA, SC, SD, SE, SG, SK, SL, SM, ST, SV, SY, TH, TJ, TM, TN, TR, TT, TZ, UA, UG, US, UZ, VC, VN, ZA, ZM, ZW.

(84) Designated States *(unless otherwise indicated, for every kind of regional protection available)*: ARIPO (BW, GH, GM, KE, LR, LS, MW, MZ, NA, RW, SD, SL, ST, SZ, TZ, UG, ZM, ZW), Eurasian (AM, AZ, BY, KG, KZ, RU, TJ, TM), European (AL, AT, BE, BG, CH, CY, CZ, DE, DK, EE, ES, FI, FR, GB, GR, HR, HU, IE, IS, IT, LT, LU, LV, MC, MK, MT, NL, NO, PL, PT, RO, RS, SE, SI, SK, SM, TR), OAPI (BF, BJ, CF, CG, CI, CM, GA, GN, GQ, GW, KM, ML, MR, NE, SN, TD, TG).

WO 2018/106828 A1

(54) Title: SYSTEM AND METHOD FOR MAGNETIC RESONANCE MAPPING OF PHYSICAL AND CHEMICAL CHANGES IN CONDUCTING STRUCTURES

FIG. 1(D)



(57) Abstract: A method of diagnosing a conducting structure includes providing the conducting structure in a magnetic field, immersing the conducting structure in a detection medium, or placing a detection medium in the vicinity of the conducting structure, exciting nuclear or electronic spins within the detection medium using a broad-band excitation pulse, receiving an NMR or ESR spectrum from the detection medium, obtaining a frequency distribution of the detection medium, and indirectly measuring internal characteristics of the conducting structure by characterizing frequency changes in the frequency distribution. Conducting structures are analyzed on the basis of changes in magnetic susceptibilities and internal electric current distributions, which may change over the course of a charging/discharging cycle, and a result of degradation and failure of the conducting structure. The conducting structure may be, for example, a battery, a capacitor, a supercapacitor, a fuel cell, or a catalyst material.

[Continued on next page]

Declarations under Rule 4.17:

— *as to applicant's entitlement to apply for and be granted a patent (Rule 4.17(ii))*

— *as to the applicant's entitlement to claim the priority of the earlier application (Rule 4.17(iii))*

Published:

— *with international search report (Art. 21(3))*

SYSTEM AND METHOD FOR MAGNETIC RESONANCE MAPPING OF PHYSICAL AND CHEMICAL CHANGES IN CONDUCTING STRUCTURES

Cross-Reference to Related Applications

[0001] This application claims priority to U.S. Provisional Application No. 62/431,075, filed December 7, 2016, which is incorporated herein by reference in its entirety for all purposes.

Field of the Invention

[0002] This application generally relates to detecting physical and chemical changes in conducting structures. In particular, this application relates to using magnetic resonance to indirectly measure internal characteristics of a conducting structure. The conducting structure may be a battery, a capacitor, a supercapacitor, a fuel cell, or a catalyst material.

Background of the Invention

[0003] Batteries are a crucial enabling technology in many important energy solutions and they are integral to advances in portable electronics, electric vehicles and grid storage. Continued demand for batteries with high energy capacity and the desire to quickly charge and discharge the devices present a number of formidable engineering and scientific challenges. Ensuring device safety is an important consideration, which needs to be addressed with care. Several industry leaders have experienced unforeseen setbacks due to battery and cell malfunctions (e.g., swelling issues). One major reason for the recurrence of such problems, and for the slow progress in battery technology is the difficulty in tracking defects inside the cells during operation in a nondestructive fashion.

[0004] Studying commercial battery designs under their typical operating conditions using conventional analytical tools has proven to be very difficult due to the large size, complicated structure and material properties of these devices. Due to these limitations, most studies have been restricted to specialized cell designs with properties amenable to study using specific techniques. These restrictions have meant that the investigation of performance and failure mechanisms in batteries is still performed destructively by cycling multiple cells and taking them

apart at critical points to analyze changes that have occurred. This process involves considerable time, effort and expense. Moreover, physical and chemical changes occurring when the cell is taken apart can compromise any information obtained.

[0005] X-Ray CT is a successful technique for scanning electrochemical cells, but it is relatively slow, and thus usually not applicable for high throughput or *in situ* applications. Furthermore, X-Ray CT provides diagnostics mostly of the denser components of a cell, and does not offer insights into subtle chemical or physical changes of the materials inside. A recently-developed acoustic technique appears to be a highly promising methodology for the non-destructive characterization of cell behavior throughout the cell life, and is currently being investigated for its sensitivity to important cell behavior.

[0006] Nuclear Magnetic Resonance (NMR) and Magnetic Resonance Imaging (MRI) have become popular methods for studying battery materials. NMR and MRI are able to probe a range of physical and chemical characteristics in situ, albeit in cell housings designed specifically for the experiments.

[0007] In magnetic resonance imaging, localization is performed with the help of magnetic field gradients. Electromagnetic radiation decays exponentially when it enters a conducting region with a characteristic length, called the skin depth,

$$\delta = \sqrt{\frac{1}{\pi \mu \nu \sigma}} \quad \text{(Equation 1)}$$

where ν is the frequency of the field, μ the permeability of the conductor and σ its conductivity. This effect has profound implications for the sensitivity of magnetic resonance (MR) techniques, which rely on radio frequency (rf) fields to excite and detect precessing spins from within conducting regions.

[0008] A key feature Equation 1 above is the dependence on $\nu^{-1/2}$ which means that at higher frequencies (corresponding to experiments performed at higher magnetic fields) δ is reduced. For example, $\delta = 12.3\ \mu$m for nuclear spins of Lithium-7 (^{7}Li) in metallic lithium at a magnetic

field of a 9.4 T (larmor frequency, $\nu_n = 155$ MHz) while Lithium-6 (^{6}Li) nuclei in the same sample will have a larger effective skin depth, $\delta = 20.0\ \mu$m because of the lower gyromagnetic ratio of this isotope and therefore lower larmor frequency ($\nu_n = 59$ MHz). For a corresponding electron spin transition, GHz frequencies would be relevant, and the skin depth would be in the range $\delta \approx 1\mu$m.

[0009] The prospect of applying magnetic resonance techniques (e.g., NMR and MRI) to commercial batteries is restricted because under typical operating conditions, conductors are not transparent to radiofrequency (rf) irradiation. Almost every cell design is encased in a conductive material, for example, solid stainless steel, aluminum, aluminum-laminated films used in pouch cells, etc. In addition, the electrodes preclude the use of conventional MR for realistic or commercial-type cell geometries. The rf fields used in typical magnetic resonance experiments are incapable of penetrating the conductive material (i.e., metallic layer) in order to excite and detect the nuclear magnetization. Nonetheless, MR has provided important insights into electrolyte behavior, Li-dendrite growth, and other electrochemical effects by the use of custom-built cells, which allow convenient rf access.

[0010] A need exists for improved technology capable of applying magnetic resonance techniques to measure physical and chemical changes in conducting structures, including batteries encased in a conductive material.

Summary of the Invention

[0011] In one implementation, a method of diagnosing a conducting structure includes providing the conducting structure in a magnetic field, immersing the conducting structure in a detection medium, exciting nuclear or electronic spins within the detection medium using an electromagnetic signal having a first frequency, receiving an electromagnetic signal having a second frequency from the detection medium, obtaining a frequency distribution of the detection medium, and indirectly measuring internal characteristics of the conducting structure by characterizing frequency changes in the frequency distribution. The conducting structure may be a battery, a capacitor, a supercapacitor, a fuel cell, or a catalyst material.

[0012] In another implementation, a method of diagnosing a conducting structure includes providing the conducting structure in a magnetic field, providing a sample including a detection medium at a predetermined distance from the conducting structure, exciting nuclear or electronic spins within the detection medium using an electromagnetic signal having a first frequency, receiving an electromagnetic signal having a second frequency from the detection medium, obtaining a frequency distribution of the detection medium, and indirectly measuring internal characteristics of the conducting structure by characterizing frequency changes in the frequency distribution. The conducting structure may be a battery, a capacitor, a supercapacitor, a fuel cell, or a catalyst material.

[0013] In a further implementation, a system for diagnosing internal characteristics of a conducting structure includes an NMR/MRI magnet, at least one radiofrequency coil removably positioned within the NMR/MRI magnet, a holder configured to receive a conducting structure, and a detection medium. The internal characteristics of the conducting structure are indirectly measured by exciting nuclear or electronic spins within the detection medium using an electromagnetic signal having a first frequency, receiving an electromagnetic signal having a second frequency from the detection medium, obtaining a frequency distribution of the detection medium, and characterizing frequency changes in the frequency distribution. The conducting structure may be a battery, a capacitor, a supercapacitor, a fuel cell, or a catalyst material. The holder containing the conducting structure may be provided inside of the detection medium or at a predetermined distance outside of the detection medium.

[0014] In yet another implementation, a system for diagnosing internal characteristics of a conducting structure includes a holder configured to receive a conducting structure; a plurality of containers arranged in three dimensions around the holder and a predetermined distance from the holder, each container housing a volume of a detection medium; a plurality of radiofrequency coils, each radiofrequency coil surrounding a container; and a plurality of detection circuits, each detection circuit connected to a radiofrequency coil. Internal characteristics of the conducting structure are indirectly measured by acquiring an NMR chemical shift spectrum to estimate a change in a magnetic field in a vicinity of each container housing the detection medium to

generate an overall field map and fit the overall field map against a calculated susceptibility distribution. The conducting structure may be a battery, a capacitor, a supercapacitor, a fuel cell, or a catalyst material.

Brief Description of the Figures

[0015] The foregoing and other objects, aspects, features, and advantages of the disclosure will become more apparent and better understood by referring to the following description taken in conjunction with the accompanying drawings, in which:

[0016] Fig. 1(A) illustrates a system for magnetic resonance mapping of physical and chemical changes in a battery including a poach cell battery.

[0017] Fig. 1(B) illustrates a holder that housing a detection medium and keeps the battery of Fig. 1(A) in place relative to the detection medium.

[0018] Fig. 1(C) illustrates a cross-section through the holder showing a first detection medium chamber, a second detection medium chamber, and a battery chamber.

[0019] Fig. 1(D) illustrates the battery and holder of Figs. 1(A) and 1(B) disposed within a radiofrequency coil positioned at an isocenter of an NMR/MRI magnet. The relative orientations of the B_0 and B_1 fields are shown relative to the object geometry in (C), with B_1 aligned with the major face of the pouch cell.

[0020] Fig. 1(E) illustrates a field map of a cell provided by the Rochester Institute of Technology (RIT cell). The RIT cell includes NMC ($Li_xNi_yMn_yCo_{1-2y}O_2$) as the cathode material. The field map is referenced to the empty holder, giving an absolute field map for the Li-ion cell.

[0021] Fig. 1(F) illustrates a field map of a commercial cell, which includes LCO (Li_xCoO_2) as the cathode material. The field map is referenced to the empty holder, giving an absolute field map for the Li-ion cell.

[0022] Fig. 2 illustrates reconstructed magnetic field maps surrounding the battery as it is discharged *in situ*. The discharge level is indicated in reference to the discharge capacity. The map for the fully charged battery (top left) is shown after subtraction of the background field map (top left colorbar), while the rest of the maps are given relative to the field map of the 0 mAh, fully charged battery (bottom right colorbar). The approximate position of the battery is illustrated in the top left image.

[0023] Fig. 3 illustrates values for the magnetic susceptibility of the whole battery obtained by fitting the sagittal imaging slices from Fig. 2.

[0024] Fig. 4 illustrates fitted susceptibilities of the left and right sides of the battery during the *in situ* charge/discharge cycle at a rate of 0.5C inside the NMR magnet. The voltage curve is displayed for the same time period (top).

[0025] Fig. 5 illustrates an "in medium" setup, an "out of medium" setup, and a "spectroscopic" setup for indirectly diagnosing the health of a battery by characterizing a frequency distribution of a detection medium.

[0026] Fig. 6 illustrates one embodiment of a computer system for implementing an embodiment of the methods described herein.

[0027] Fig. 7 illustrates a pixel-wise difference between the left and right hand sides of the magnetic field maps from Fig. 2, which were obtained *ex situ* during cell discharge.

[0028] Fig. 8 illustrates sagittal snapshots of the field maps during the *in situ* discharge/charge cycle.

[0029] Fig. 9 illustrates a series of magnetic field maps taken at intervals during discharge and then charge of the cell. The plots are labeled by the discharge capacity of the cell at each step. The magnetic field is displayed with the fully charged cell as reference. The RIT cell was used for this purpose, and the susceptibility increased upon discharge.

[0030] Figs. 10(A) – 10(B) illustrate fitted magnetic susceptibilities of the cell during the discharge/charge. For simplicity, the cell is assumed to have an average volume susceptibility in Fig. 10(A). Error bars are smaller than the size of the points. Knowing the cell construction, one can, however, also determine the average susceptibility of the cathode material in Fig. 10(B). The susceptibility values are given in ppm indicating a factor of 10^{-6}.

[0031] Fig. 11 illustrates magnetic field maps for the defect cells, with the mean and standard deviation indicated (taken over all of the voxels in each image). The fields are given relative to one of the non-defect cells (not shown).

[0032] Fig. 12 illustrates the principal component analysis performed on the magnetic field maps of the cells shown in Fig. 11.

[0033] Fig. 13 illustrates the susceptibility fitting process for the fully charged commercial cell.

[0034] In the following detailed description, reference is made to the accompanying drawings, which form a part hereof. In the drawings, similar symbols typically identify similar components, unless context dictates otherwise. The illustrative embodiments described in the detailed description, drawings, and claims are not meant to be limiting. Other embodiments may be utilized, and other changes may be made, without departing from the spirit or scope of the subject matter presented here. It will be readily understood that the aspects of the present disclosure, as generally described herein, and illustrated in the figures, can be arranged, substituted, combined, and designed in a wide variety of different configurations, all of which are explicitly contemplated and made part of this disclosure.

Detailed Description of the Invention

[0035] In general, the system and method described in this application relate to indirectly detecting the conductivity distribution and the distribution of magnetic susceptibility of conducting structures by measuring the space around it with NMR spectroscopy or MRI. In the embodiments described in this application, the conducting structure is a battery. However, the present application is not limited in this regard. The conducting structure may be, for example, a

capacitor, a supercapacitor, a fuel cell, a catalyst material, etc. The system and method described herein provides cell diagnostics without requiring rf access to the inside of the cell. The method is based on imaging the induced or permanent magnetic field produced by the cell, and connecting it with processes occurring inside the cell. A method of diagnosing a battery includes providing the battery in a magnetic field, immersing the battery in a detection medium, or placing a detection medium in the vicinity of the battery, exciting nuclear or electronic spins within the detection medium using a broad-band excitation pulse, receiving an NMR or ESR spectrum from the detection medium, obtaining a frequency distribution of the detection medium, and indirectly measuring internal characteristics of the battery by characterizing frequency changes in the frequency distribution. Batteries are analyzed on the basis of changes in magnetic susceptibilities, a measure of the degree of magnetization of a material when a magnetic field is applied, and internal electric current distributions, which may change over the course of a charging/discharging cycle, and a result of battery degradation and failure. The reason that this magnetic field is so informative, is that the magnetic susceptibility χ is material-dependent, and that the resulting magnetic field is dependent on the distribution of the materials inside of the cell, which change during cell operation.

[0036] The magnetic susceptibility also depends on the electronic configuration of the material and hence during redox reactions, such as battery charging or discharging, there can be large changes in magnetic susceptibility. Measurements of magnetic susceptibility can therefore yield detailed information about the oxidation state of the materials inside an electrochemical device to give insights into the state of charge (SOC) of the battery and its failure mechanisms. Furthermore, the magnetic susceptibilities of many widely-used electrode materials, including, for example Li_xMnO_2, Li_xFePO_4, Li_xCoO_2 and $Li_xNi_yMn_yCo_{1-2y}O_2$, depend upon their lithiation state. Graphite, a popular anode material, is strongly diamagnetic and has a highly anisotropic susceptibility. In this case, as Li^+ intercalates into the structure, the inter-layer distance in the graphite increases and the susceptibility and its anisotropy are significantly reduced. This effect is highly dependent on the stage (the number of graphite layers between each lithium layer) of the resulting lithium intercalate.

[0037] Monitoring the magnetic field produced by the cell when it is placed into an external magnetic field thus offers the ability to monitor the electrochemical reaction *in situ*. Moreover, the distribution of magnetic material inside the cell influences the spatial variation in the magnetic field that it produces, such that it is also sensitive to the precise construction of the cell. In this manner, measures of the magnetic field can be used to screen for physical defects in cells.

[0038] MR methods provide the ability to measure tiny changes in magnetic field maps, for example, through the use of phase-map imaging or specific NMR probes. In the phase-map imaging approach, multiple images are acquired at different echo times and used to reconstruct the spatial variation in the induced resonance frequency shift from the evolution of the signal phases. In this manner, very accurate field maps can be obtained - of the order of μT. Since ultimately, the magnetic field changes are measured, apart from measuring the magnetic properties of a device, one could also measure current distributions in the same manner, which could arise, for example, in the relaxation phase between charging steps, or during charging or discharging itself.

[0039] Referring to Figs 1(A)-1(D), a system 100 for magnetic resonance mapping of physical and chemical changes in a battery 200 includes a holder 10 configured to receive the battery 200, a radiofrequency coil 20, and an NMR/MRI magnet 30. In use of the system 100, the holder 10 is disposed within the radiofrequency coil 20. The radiofrequency coil 20 is then disposed within an isocenter of the NMR/MRI magnet 30. In some examples (e.g., Figs. 1(A)-1(D)), the holder 10, the radiofrequency coil 20, and the NMR/MRI magnet 30 are concentric. In other examples (e.g., Fig. 5C), the holder 10, the radiofrequency coil 20, and the NMR/MRI magnet 30 are not concentric. The radiofrequency coil 20 can be repeatedly removed and inserted within the NMR/MRI magnet 30. The holder 10 can be repeatedly removed and inserted within the radiofrequency coil 20. The system 100 may also include a spectrometer containing a gradient assembly and/or an imaging probe.

[0040] The holder 10 may be made of any non-magnetic material. For example, the holder 10 may be made of plastic such as poly lactic acid (PLA) plastic or acrylonitrile butadiene styrene (ABS) plastic. The holder 10 may be manufactured in any manner, for example, by 3D printing.

In the example of Fig. 1(B), the holder 10 is cylindrical and partitioned into three portions: a first detection medium chamber 11, a second detection medium chamber 12, and a battery chamber 13 that separates the first detection medium chamber 11 and the second detection medium chamber 12. In other examples, the holder 10 is not cylindrical. For example, the holder 10 may have a square, obround, ovular, rectangular or otherwise oblong cross section.

[0041] The first detection medium chamber 11 and the second detection medium chamber 12 are configured to be filled with a same volume and same kind of detection medium. Each of the first detection medium chamber 11 and the second detection medium chamber 12 extends from a top of the holder 10 to a bottom of the holder 10. The detection medium may be, for example, water or water doped with a paramagnetic species (e.g., $CuSO_4$, Gd-DTPA), to shorten the T1 relaxation times for faster measurements. Other examples of a detection medium that may be used include oil or tetramethyl silane. Any detection medium may be used provided the detection medium is MR active and compatible with the material from which the holder 10 is made. The minimal requirement for the detection medium is to contain a sufficient concentration of nuclear or electronic spins leading to a strong enough magnetic resonance signal. For the detection medium, liquids are preferred because they produce narrow lines with high signal-to-noise ratios, but in some examples, it may be possible to use gas as a detection medium. The ideal detection medium would also produce only a single resonance in the frequency spectrum with little internal interactions. An example is liquid water with ^1H nuclear spins, which produces a very strong signal. Solids could also be used as the detection medium, but a high symmetry solid would be desired in order to minimize internal interactions, such as chemical shift anisotropy. Solids could be relevant for high-temperature applications. A low electric permittivity can increase the range of the detectable magnetic fields. Such a sample could be constructed from an oil sample, for example. It is advantageous to select a detection medium that provides a maximum MR signal (this is achieved, for example, by using a high-density liquid such as water as the detection medium).

[0042] In examples in which the detection medium is water doped with a paramagnetic species, the paramagnetic species may increase spin-lattice relaxation, and thus, the experiments could be

sped up. One can typically choose a concentration regime where $T_2^* < T_2$ such that the signal amplitude is not significantly compromised due to excessive line broadening introduced by the paramagnetic species. The first detection medium chamber 11 and the second detection medium chamber 12 are configured to be sealed during use of the system 100.

[0043] The battery chamber 13 is configured to receive the battery 200 to be evaluated by the system 100. In the example of Fig. 1(B), the battery chamber 13 is a rectangular slot in a central portion of the holder 10. The battery chamber 13 extends from the top of the holder 10 to a position above the bottom of the holder 10. In other words, the battery chamber 13 does not extend to the bottom of the holder 10. The battery chamber 13 may be configured to receive a capacitor, a supercapacitor, a fuel cell, or a catalyst material.

[0044] In the example of Fig. 1(A), the battery 200 is a pouch cell battery having electrodes 210 extending from a top surface thereof. When the battery 200 is received by the battery chamber 13, the battery 200 is oriented such that the electrodes 210 are proximal to the top surface of the holder 10 and the bottom surface of the battery 200 is distal to the top surface of the holder 10. At least a portion of the battery 200 rests on a bottom surface of the battery chamber 13. A first space exists between a top of the battery 200 and the top of the holder 10. A second space exists between a bottom of the battery 200 and the bottom of the holder 10. By having the length of the battery 200 shorter than the length of the first detection medium chamber 11 and the second detection medium chamber 12 containing the detection medium, a more uniform magnetic field can be observed across the detection medium. This is not essential, however, as in other examples, the battery chamber 13 may extend an entire length of the holder 10 and the battery 200 may have a length greater than or equal to the length of the first detection medium chamber 11 and the second detection medium chamber 12 containing the detection medium. In some examples, it may be preferable to have the detection medium extend over a length of about 1/3 of the battery length at both the top and the bottom. The battery holder 10 is configured to fill the available volume of the radiofrequency coil 20 (e.g., a cylindrical space having dimensions, for example, of a 40mm diameter and a 60cm height 60 cm), while keeping the battery 200 centered. This setup allows for the largest area around the battery 200 to be

mapped and compared to calculations for ascertaining the magnetic susceptibility of the battery 200, and therefore, in most cases, this setup will be optimal. If a smaller battery is evaluated, the size of the first detection medium chamber 11 and the second detection medium chamber 12 containing the detection medium would be the same, but the size of the battery chamber 13 would be reduced. The top surface of the battery chamber 13 is configured to remain unsealed during use of the system 100, to allow access to the electrodes 210 during evaluation of the battery 200.

[0045] The size of the holder 10 and the shape and size of the battery chamber 13 may be modified/customized to receive different shapes and sizes of batteries.

[0046] A method for magnetic resonance mapping of physical and chemical changes in a battery using the system 100 will now be described. The method includes using magnetic resonance to indirectly measure internal characteristics of a battery. Instead of detecting physical and chemical changes of the battery by directly imaging the battery, the method of the present application involves detecting changes in the detection medium that surrounds the battery and using the data to reconstruct information about the chemical and physical changes occurring inside of the battery. The detectable changes may originate from changes in magnetic susceptibilities, leading to alterations of induced magnetic moments, from changes in the permanent magnetism inside the cell, or from changes in the current distribution inside the battery.

[0047] The changes in the oxidation states of the electrochemically active ions and components of the electrode materials are intrinsic processes occurring in electrochemical devices. These changes can impact the local structure and other properties, such as their local magnetic properties. For example, the lithiation state in Li_xCoO_2, a common cathode material, is closely tied to the electronic structure of the Cobalt ion in the rigid CoO_2 layers. See Hertz, J. T.; Huang, Q.; McQueen, T.; Klimczuk, T.; Bos, J. W. G.; Viciu, L.; Cava, R. J. *Phys. Rev. B*, *77* (7), 75119 (2008), the entire contents of which is hereby incorporated by reference for all purposes including for the disclosures related to examples of how the magnetic susceptibility of electrode materials change upon lithiation. The Co^{4+} ions change from high spin (5 unpaired

electrons) when $x \geq 0.97$ to low spin (1 unpaired electron) for $0.50 \leq x \leq 0.78$, and there is an accompanying increase in the magnetic susceptibility of the material by an order of magnitude. Examples of these processes include, for example, effects in carbon anodes/$LiFePO_4$ (see Kadyk, T.; Eikerling, M. *Phys Chem Chem Phys*, *17* (30), 19834–19843 (2015), the entire contents of which is hereby incorporated by reference for all purposes including for the disclosures related to examples of how the magnetic susceptibility of electrode materials change upon lithiation), and NiMnCo cathode materials (see Chernova, N. A.; Ma, M.; Xiao, J.; Whittingham, M. S.; Breger, J.; Grey, C. P. *Chem. Mater.* *19* (19), 4682–4693 (2007), the entire contents of which is hereby incorporated by reference for all purposes including for the disclosures related to examples of how the magnetic susceptibility of electrode materials change upon lithiation).

[0048] First, the first detection medium chamber 11 and the second detection medium chamber 12 of the holder 10 are filled with a desired detection medium and sealed. The battery 200 is then inserted into the battery chamber 13 of the holder 10. Next, the holder 10 is disposed within the radiofrequency coil 20. The radiofrequency coil 20 is then disposed within the isocenter of the NMR/MRI magnet 30. The battery 200 may be evaluated *ex situ* (i.e., charge/discharge stopped data acquisition) and/or *in situ* (i.e., a current is applied such that charge/discharge occur during data acquisition). A static magnetic field B_0 is applied. The nuclear or electronic spins within the detection medium are excited using a broad-band excitation pulse (e.g., a RF frequency for nuclear spins). A phase map is acquired and processed as described below in order to obtain a frequency distribution within the detection medium. The measurements are performed either during charging or discharging of the battery, either while current is flowing, or while current is stopped.

[0049] In one example, the internal characteristics of the battery are modeled on the basis of magnetic susceptibility differences and changes within the battery. This is accomplished by assigning one or several regions within the battery a given magnetic susceptibility and calculating the effect on the surrounding medium. The susceptibilities of the different regions form parameters that can be fit by minimizing the differences between the calculated and the measured frequency distributions in the surrounding detection medium or the detection volume.

[0050] From the observed frequency changes in the frequency distribution, it is possible to infer the overall changes in magnetic susceptibility distributions within the battery. This is important in the context of studying the health and general state of a battery and could be relevant for studying battery failure mechanisms and quality control. In particular, data from a standard MRI phase map is processed to measure the symmetry of the collected image. The symmetry of the collected image is then compared to a predetermined standard acceptable symmetry. The symmetry of the materials inside the battery is indicative of failure mechanisms, quality control during production (e.g., indicative of whether the manufactured batteries fall within an acceptable range of symmetry) and information about the efficiency of the cell during cycling. With regards to cell cycling, the comparison will indicate whether some regions of the battery are cycling more efficiently than others due to local hotspots in the electric current. This information can be obtained based solely on the frequency distribution of the detection medium (i.e., without opening the battery or measuring the battery directly).

[0051] A pixel comparison of the difference between the left and right hand sides of the magnetic field map may also be used to infer the overall changes in magnetic susceptibility distributions within the battery. Fig. 7 illustrates the results of taking a pixel-wise difference between the left and right hand sides of the magnetic field maps from Fig. 2, which were obtained ex situ during cell discharge. The discharge level is indicated in reference to the discharge capacity. The background field is subtracted from each map prior to taking the difference.

[0052] In another example, the internal characteristics of the battery modeled on the basis of current distributions within the battery. This is accomplished by assigning one or several regions within the battery volume given current distributions. From the currents, the generated magnetic fields are calculated and their effects on the surrounding medium are determined. The current amplitudes assigned to different regions in the battery form parameters that can be fit by minimizing the differences between the calculated and the measured frequency distributions in the surrounding detection medium or the detection volume.

[0053] In the examples in which the internal characteristics of the battery are modeled on the basis of magnetic susceptibility differences and changes within the battery, or current distributions within the battery, the state of charge (SOC) of the battery is determined by converting the determined frequency distributions into the state of charge. In conventional diagnosis methods, intact batteries are diagnosed by measuring their voltage and resistance/impedance. These values can be related to state of charge (SOC) by making calibration curves for the battery in a similar way. However, as the battery ages, the calibration changes and so mathematical models need to be included that account for aging. However, this requires some knowledge of the battery history, such as cycle life/battery health. By measuring the detection medium, as opposed to the voltage and resistance/impedance of the battery itself, it is possible to provide an independent measure of the SOC. If desired, the independent measure of the SOC may be combined with the voltage/resistance measurements to double-check the SOC and battery health.

[0054] Several experiments were performed, as described below.

EXPERIMENTAL SETUP

[0055] In the experiments, the holder was 3D printed using PLA plastic. The detection medium selected was water. The battery was a non-magnetic PGEB-NM053040 lithium polymer pouch cell having a rated capacity of 600 mAh and a measurement of 5 mm x 30 mm x 40 mm. Prior to the experiments, the battery (i.e., the pouch cell) was fully charged by applying 120mA (0.2C) current until the cutoff voltage of 4.2 V was reached.

MRI EXPERIMENTS

[0056] The MRI experiments were performed on a Bruker Ultrashield 9.4 T Avance I spectrometer containing a Bruker Mini0.75 gradient assembly and operating at 400.1 MHz for 1H. A Bruker MiniWB57 imaging probe was used to collect the data, with a Bruker WB57 40 mm inside diameter (i.d.) coil insert for ^{1}H experiments. 2D and 3D gradient echo experiments were performed using the FLASH sequence implemented in Paravision 5.1.

[0057] For the 2D experiments, a 1 mm slice was acquired with a 51.2 x 51.2 mm square field of view (FOV) with 128 points in both the read and phase dimensions, to give a nominal resolution of 0.4 x 0.4 mm. The slice was taken perpendicular to the major face of the battery (hereinafter the "sagittal plane"), which is illustrated in Fig. 1(D). Spatial encoding using the readout gradient was performed in the vertical (z) direction which gave fewer artifacts from the detection medium outside the FOV. For the *ex situ* experiments, a nominal flip angle (α) of 15° was used with a repetition time (TR) of 100 ms. The *ex situ* experiment took 2 min 33 s, with 12 averaging scans (NS) acquired. For *in situ* experiments, a nominal flip angle (α) of 10° was used with a repetition time (TR) of 40 ms. The *in situ* experiment took 20s, with 4 averaging scans (NS) acquired. Reasonable experiment times were chosen and then the flip angles can be taken as slightly less than the Ernst angle ($\alpha \leq \alpha_E = \cos^{-1}(e^{-TR/T1})$ with T_1=2.5 s for water). For the in situ and 3D experiments it was important to minimize the experiment time, and TR and α were reduced accordingly. Additional parameter tests were performed to maximize the signal to noise ratio (SNR) for a given experiment time.

[0058] The 3D experiments used an isotropic 51.2 mm FOV with 128 points in each dimension to give a nominal, isotropic resolution of 0.4 mm. For the 3D experiments, a nominal flip angle (α) of 5° was used with a repetition time (TR) of 15 ms. The 3D experiment took 4 min 5 s, with 1 averaging scan (NS) acquired. The 3D experiments measure the same properties (a phase map) as the 2D experiments, but in all three spatial dimensions. Only two spatial dimensions are mapped in the 2D experiments, with slice selection used during the rf excitation to localize the maps to a single slice in the third dimension. 3D measurements could provide additional accuracy.

[0059] The experiments were repeated at multiple echo times (TEs) from a minimum of 2.45 ms, and the image series used to reconstruct the local field map surrounding the battery, as detailed below.

IMAGE PROCESSING

[0060] The purpose of the gradient echo MRI experiments is to obtain the true phase maps, $\theta(r)$, of the detection medium. However, the detection of NMR or MRI is limited to the range $(-\pi, \pi]$, and so any regions of the measured phase maps, $\theta_{\mathrm{wr}}(r)$, that lie outside of this range will be wrapped, $\theta_{\mathrm{wr}}(r) = \theta(r) - 2\pi n(r)$. To recover the true phase maps, the integer wrapping parameters, $n(r)$, must be obtained. In general, the accumulated phase is proportional to the TE used in the experiment, $\theta(r, \mathrm{TE}) = \theta_{\mathrm{rec}}(r) + \omega(r) \cdot \mathrm{TE}$, where ω(r) is the angular frequency offset relative to the carrier frequency of the rf pulse used and $\theta_{\mathrm{rec}}(r)$ is an additional, static phase offset caused by the receiver. The time-dependent effects of nutation can be isolated by comparing the phase difference between two consecutive echoes, $\delta\mathrm{TE}_{i+1,i} = \mathrm{TE}_{i+1} - \mathrm{TE}_i$, so that $\delta\theta_{i+1,i}(r) = \omega(r) \cdot \delta\mathrm{TE}_{i+1,i}$ (where the i subscript indicates the echo number). The consecutive echoes can be obtained from a multi-echo acquisition after a single excitation, or from separate experiments. The former approach allows for a more rapid overall acquisition but results in longer $\delta\mathrm{TE}_{i+1,i}$ times due to the need for additional gradients to be applied. The latter approach, used here, has the advantage of allowing arbitrarily small values for $\delta\mathrm{TE}_{i+1,i}$, limited only by the effective clock speed of the spectrometer, which is typically of the order of 1 μs or less. Minimizing $\delta\mathrm{TE}_{21}$ reduces the occurrence of phase wrapping between the consecutive scans.

[0061] Following roughly the methodology of the UMPIRE algorithm (Robinson, S.; Schödl, H.; Trattnig, S. *Magn. Reson. Med. Off. J. Soc. Magn. Reson. Med. Soc. Magn. Reson. Med.*, *72* (1), 80–92 (2014), the entire contents of which is hereby incorporated by reference), experiments were obtained at four different TEs, $\mathrm{TE}_1 = 2.45$ ms, $\mathrm{TE}_2 = 2.50$ ms, $\mathrm{TE}_3 = 2.75$ ms and $\mathrm{TE}_4 = 2.80$ ms. By converting each image, S_i to a phase map,

$$\theta_{\mathrm{wr}}^{i}(r) = \tan^{-1}[\mathrm{Im}(S_i(r))/\mathrm{Re}(S_i(r))], \qquad (1)$$

the difference maps $\delta\theta_{21}(r)$, $\delta\theta_{32}(r)$ and $\delta\theta_{43}(r)$ can be obtained and used to calculate three estimates of $\omega(r)$. The median value of $\omega(r)$ is then used to find the integer coefficients $n_{i+1,i}(r)$ that unwrap each of the phase difference images,

$$n_{i+1,i}(r) = \left\lfloor \frac{\delta\theta_{i+1,i}(r) - \delta \mathrm{TE}_{i+1,i} \cdot \omega(r)}{2\pi} \right\rfloor, \quad (2)$$

where the brackets denote the floor function. Each phase difference map is unwrapped accordingly,

$$\delta\theta'_{i+1,i}(r) = \delta\theta_{i+1,i}(r) - 2\pi n_{i+1,i}(r). \quad (3)$$

From the set of unwrapped phase difference maps we can obtain a second, more accurate estimate of $\omega(r)$, again by taking the median of the values from the three phase difference images. Eqs 2 and 3 can then be used to unwrap the original phase maps and obtain the true phase maps, $\theta(r)$, at each of the echo times.

[0062] One aspect of interest is the field map, which is expressed in units of ppm relative to the Larmor frequency, ν_0, of the ^{1}H nuclear spin (400.13 MHz at the 9.4T field used in the experiments), $\Delta B_0(r) = (\omega(r)/2\pi) \cdot (10^6/\nu_0)$. While this quantity could be calculated directly from the most accurate estimate of $\omega(r)$ obtained from the difference maps, pixel-wise least square fits of $\theta(r)$ as a function of TE can provide more accurate values incorporating all of the data. Moreover, the total least squares error on each fit can be used to discriminate between pixels where the unwrapping procedure has or has not worked. In the pixels where the unwrapping procedure failed, typically 10-20 pixels per image, a nearest-neighbor smoothing algorithm was used to assign $\Delta B_0(r)$.

[0063] The results from the gradient echo experiments were converted into an unwrapped phase map, and finally to a magnetic field map via the UMPIRE algorithm. The magnetic susceptibility of the battery is calculated from the field map by comparing the experimentally obtained $\Delta B_0(r)$ map with calculation. In particular, the field map surrounding a model battery geometry matching the powerstream cell was calculated using the FFT method, with the same FOV (zero filled) as the experimental image. The FFT method is described, for example, in Salomir, R.; de Senneville, B. D.; Moonen, C. T. *Concepts Magn. Reson., 19B* (1), 26–34 (2003), and Ilott, A. J.; Chandrashekar, S.; Klöckner, A.; Chang, H. J.; Trease, N. M.; Grey, C. P.; Greengard, L.; Jerschow, A. *J. Magn. Reson. 245*, 143–149 (2014), the entire contents of which

are hereby incorporated by reference. The susceptibility value for the battery was fitted using a Python program to minimize the difference between the simulated and experimental phase maps. A single (volume) susceptibility is used to describe the whole battery in these examples, although further battery-specific models could be used, wherein different susceptibilities are assigned to different regions within the battery.

RESULTS

[0064] Figs. 1(E) and 1(F) illustrate field maps measured for the cells. In particular, Fig. 1(E) illustrates a field map of a cell provided by the Rochester Institute of Technology (RIT cell) that includes NMC ($Li_xNi_yMn_yCo_{1-2y}O_2$) as the cathode material. Fig. 1(F) illustrates a field map of a commercial cell that includes LCO (Li_xCoO_2) as the cathode material. As evidenced by Figs. 1(E) and 1(F), the system and method described herein can work with different types of cells. For the RIT cell experiment, the exact information about all the battery components and materials were known. However, such information was not available for the commercial cell. Thus, the RIT cell experiment provides validation of the technique and demonstrating that it is possible to calculate absolute cathode magnetic susceptibility values, as the "known" information was available to corroborate the results. The use of the RIT cell also enabled the focus and proof of concept for application of systems described herein for diagnosis of specific defects of cells.

[0065] The field maps are referenced to the empty holder, giving an absolute field map for the Li-ion cell. Only the magnetic field in the plane perpendicular to the main face of the cell is displayed for clarity. The map shows a 1-2 ppm change in the field due to the magnetic properties of the battery. This change in field is large in comparison to the typical resolution limit of phase mapping methods, where it has been demonstrated that differences in susceptibilities of 0.1 ppm (or about 1μT) can be resolved easily. The method is insensitive to changes in the background field or fluctuations in the instrument's magnetic field because all measurements can be taken with respect to a reference image of either the holder alone, a reference cell or the initial state of the same cell. There are artifacts at the corners of the field map, as expected, where the magnetic properties change particularly rapidly, which is also due to

the presence of the leads and air pockets, but these effects are short-ranged and these regions can be neglected.

[0066] While Figs. 1(E) and 1(F) illustrate an individual measurement, Fig. 2 illustrates field maps of the commercial cell at different stages of discharge. In particular, Fig. 2 shows the reconstructed field maps for one of the batteries (commercial cell), with snapshots taken at different points during discharge. When the battery is fully charged, the local field map varies from −14 to +10 ppm. Most regions of the map are successfully reconstructed, although close to the corners of the battery there is complete cancellation of the signal. This effect is due to the rapidly changing field, and occurs where the phase changes by close to 2π or more across a single voxel. These regions impact a limited area of the map and did not compromise further analysis.

[0067] The remaining images in Fig. 2 chart the relative changes in the field map as the battery is discharged. During the initial stages of discharge (75 - 300 mAh) the changes are relatively minor, with the magnitude of the field reducing (indicating that the average magnetic susceptibility inside the battery is also reducing) within approximately 0.5 ppm of the fully charged case. The changes are accelerated at higher stages of discharge (375 - 575 mAh) until there is up to 3-4 ppm change in magnitude at the fully discharged state.

[0068] The field maps are used to estimate the average magnetic susceptibility of the materials inside of the battery (Fig. 3), as detailed in the methods section. Following the trends visible in the field maps, the fits show the susceptibility of the battery to change only slightly until 350 mAh, when there is a strong decrease to approximately 70% of the maximum value. The trends are the same on charge as on discharge, suggesting that the oxidation state of the electrode materials is the same at equivalent points on charge versus discharge. If the materials and their relative volume fractions inside the battery were known, it would be straightforward to calculate the magnetic susceptibility at each stage of lithiation for the anode and cathode, and to convert the susceptibility axis in the plot in Fig. 3 to a lithiation fraction for each material.

[0069] The curve in Fig. 3 can also be used to calibrate the measured susceptibility as an indicator of the current state of charge (SOC) of the battery. This method would be particularly effective at discharge capacities above 300 mAh where the susceptibility changes are greater, but it could be combined with voltage and other measurements to classify batteries in the initial stages of discharge. The calibration curve would be slightly different for each type of battery and constituent chemistry.

[0070] The experiments were repeated *in situ* on a second (fresh) cell, with a charge/discharge rate of 0.5C and 30-minute rest periods after charge/discharge. The results of the consecutive imaging scans are shown in Fig. 8, which displays sagittal snapshots of the field maps during the *in situ* discharge/charge cycle. The labeled red circles on the electrochemistry plot indicate the times at which the eight images were acquired, while the smaller black squares on the voltage curve illustrate the positions of all of the images (not shown) taken during the acquisition series, demonstrating the high temporal resolution of the method. The ΔB_0 map of the fully charged battery is subtracted from the displayed field maps. The maps show an asymmetry between the left and right sides of the cell; during discharge, the right side of the map has a higher field shift than the fully charged reference image (red regions) while the left side of the map has a lower field (blue regions). During the charge period, this trend is reversed. Thus, it appears that the left and right sides of the detection medium 'see' batteries with differing magnetic susceptibilities.

[0071] To account for the spatial variation, fits of the experimental susceptibility distribution were performed separately for the left and right sides of the image, obtaining separate estimates of the battery susceptibility for each. This method was preferred to one in which each side of the battery was assigned independent susceptibilities, with the latter resulting in more time consuming and unstable fits. The results (Fig. 4) show there to be a significant, ca. 1×10^{-5} difference in battery susceptibilities obtained from the right and left sides of the battery, with the right side sensing a higher susceptibility on discharge and the left side a higher susceptibility on the subsequent charge, with a significant swing in the susceptibilities during the resting step between the two periods and subsequent reversal of the applied current direction.

[0072] This type of spatial variation is not observed in the *ex situ* results. This difference may be due to the extra time during which the battery can relax before the experiments are performed ex situ. A second possibility is that the application of the current itself results in an additional modification to the magnetic field, which could be calculated according to the Biot-Savart Law if the current distribution were known. When the current changes direction the magnetic field should also reverse, as is observed in Fig. 4. Furthermore, this explanation for the phenomenon would lead to almost instantaneous changes in the measured field when the applied current is switched on or off, as appears to be the case. Applicant believes that the field change should be proportional to the current. If the field change is due to the applied current, the effects can be isolated by measuring the field change as a function of the applied current and separating this contribution from the magnetic susceptibility effects. The result will be a magnetic field map that can be related to the current distribution inside the battery, also a unique and powerful method.

[0073] The magnetic field can be used as a diagnostic for a cell's state of charge and to measure inconsistencies and defects in a cell's construction. Fig. 9 shows the change in the field map measured around the cell at discrete steps during discharge and then charge. The maps show that the field gradually reduces during discharge, to a minimum of -1.5 ppm (14.1 μT) lower than in the fully charged cell, with the reverse trend followed on the subsequent charge steps. The changes occur in a mostly symmetric fashion, with two symmetry planes bisecting the map vertically and horizontally.

[0074] Each step in the charge/discharge profile in Fig. 9 results in a unique field map, with changes that can be readily measured. This one-to-one mapping between charge state and the measured field map can therefore provide a fast tool for recovering the state of charge of an unknown cell, which may not be available from voltage measurements for many cell types, especially if the cell is compromised. More importantly, because it is the variation in the oxidation states of the anode and cathode materials that drive the differences in the measured bulk magnetic susceptibility, the field maps can provide vital additional information about cell health.

[0075] From this data, the cell's susceptibility changes over the charge cycle can be derived. Fig. 10 shows how the bulk magnetic susceptibility changes during discharge for two types of cells. The RIT cell uses NMC ($Li_xNi_yMn_yCo_{1-2y}O_2$) as the cathode material, and it is known that the magnetic susceptibility of this material increases with lithiation level. By contrast, results are also shown for a commercial cell with LCO ($LixCoO_2$) as the cathode material. In that case, susceptibility decreases upon cathode lithiation (discharge). Both of these effects are clearly observed over a full cycle in Fig. 10(A), and can be measured precisely. The analysis shown in Fig. 10(A) is based on the simplest-possible model, the susceptibility being distributed uniformly across the cell. Knowing the geometry and the materials of the cell, however, one can obtain a more detailed analysis and extract the susceptibility changes of the cathode materials alone, which are shown in Fig. 10(B).

[0076] The susceptibility-induced modification to B_0 caused by the paramagnetic lithium metal structure inside the voxel was calculated using a FFT method according to the equation

$$h_{obj,z} = -H_0 . FT^{-1}\left[\frac{k_z^2}{k^2} . FT(\chi)\right]. \qquad (S1)$$

Susceptibility values for the cells were obtained in two different ways: (1) Average susceptibility for the whole cell: the susceptibility value was obtained by performing a numerical fit to match the experimental magnetic field map with the predicted one from the cuboid. (2) In order to obtain the cathode susceptibility, the known susceptibility values for all other components were obtained from the literature, and the volume fraction of the active cathode material was used to calculate the contribution from the cathode alone. The cell was weighed and measured to obtain the total mass and volume. Using the mean experimental susceptibility of the whole cell, the volume fraction of each component, and susceptibility values of all components except the cathode, one can calculate the susceptibility of the cathode changing by oxidation state. See Tables 1 and 2 below for the results.

[0077] Average susceptibility for the whole cell may be calculated using the following method to fit the experimental field map to recover the cell susceptibility:

1. A 3D model system, $\chi(x, y, z)$ is built to represent the susceptibility of the cell, with a cuboid representing the cell in the center of the simulation box. The simulation box is 256^3 voxels and nominally represents a volume of 102 x 102 x 102 mm with a 400 μm isotropic resolution to match the experimental conditions. A cuboid with dimensions 4.8 x 29.6 x 30.4 mm is used for the commercial cell and 2.4 x 35.2 x 51 mm for the RIT cell. The susceptibility values in the cell are set such that $\chi(\text{inside battery}) = \chi_{\text{cell}}$ and $\chi = 0$ elsewhere.
2. The FFT susceptibility calculation method is used to predict the 3D magnetic field map around the cell in the model system, $\mathrm{B}_{0,\mathrm{sim}}(x, y, z)$ (2D slide shown in Fig. 13).
3. A 2D slice of the simulated map is cropped (dotted box in Fig. 13) to match the dimensions of the experimental image. An additional mask is applied to select only regions that are non-zero in the experimental image, $B_{0,\mathrm{exp}}(x, y)$, which has been corrected by the reference image of the cell holder alone, i.e.

$$\mathrm{B}'_{0,\mathrm{sim}}(x, y) = \begin{cases} B_{0,\mathrm{sim}}(x, y), & B_{0,\mathrm{exp}}(x, y) \neq 0 \\ 0, & B_{0,\mathrm{exp}}(x, y) = 0 \end{cases}$$

4. The least squares error between the simulated and experimental field maps is calculated, $|\mathrm{B}'_{0,\mathrm{sim}}(x, y) - B_{0,\mathrm{exp}}(x, y)|$, and summed, to provide a measure of the similarity between the two maps (Fig. 13(D)).

The minimize function in the scipy package is used to fit the value of χ_{cell} by repeating the calculation. The right-hand side of Fig. 13 shows the difference between the experimental and simulation field maps for the optimally fitted value for χ_{cell}. The deviation is relatively large and illustrates the availability of further information beyond the basic model.

[0078] Using the physical measurements of the cell components and the anode susceptibility and the mean susceptibility of the cell at each state of charge, the cathode susceptibility was calculated as seen in Table 1 below. The volume fraction of each component is used to determine its contribution to the overall observed susceptibility.

TABLE 1

Discharge capacity (mAh)	Anode susceptibility χ_{volume}	Mean susceptibility of the cell χ_{volume}	Cathode susceptibility χ_{volume}
0	$-2.72 \cdot 10^{-5}$	$1.08 \cdot 10^{-4}$	$3.42 \cdot 10^{-4}$
95	$-2.28 \cdot 10^{-5}$	$1.22 \cdot 10^{-4}$	$3.78 \cdot 10^{-4}$
125	$-2.08 \cdot 10^{-5}$	$1.31 \cdot 10^{-4}$	$4.02 \cdot 10^{-4}$
185	$-6.77 \cdot 10^{-5}$	$1.52 \cdot 10^{-4}$	$4.47 \cdot 10^{-4}$
215	$5.56 \cdot 10^{-5}$	$1.65 \cdot 10^{-4}$	$4.70 \cdot 10^{-4}$
250	$3.68 \cdot 10^{-5}$	$1.66 \cdot 10^{-4}$	$4.75 \cdot 10^{-4}$

[0079] Both the spatial dependence of the oxidation state, and the distribution of the material in space also affect the bulk magnetic susceptibility. Therefore, this tool can be used to detect changes in the cell over time, as well as physical defects in a cell. Fig. 11 shows the resulting field maps when the method is applied to a series of pouch cells that are purposely defected by either folding one of the cathodes, removing a cathode altogether, or adding small scraps of electrode material into the cell construction. Not only do the measured field maps show strong differences that are indicative of the defect types, the observed changes are also intuitive and diagnostic. For example, when the electrode is folded, new features are observed in the image at the locations where the fold occurs. When there is a missing cathode, the mean value of the field noticeably increases, as would be expected. The changes are subtler when extra scraps are added to the cell, but there is a slight increase in the mean and standard deviation of the measured magnetic field. Furthermore, the MRI method is sensitive enough to resolve significant differences for even the two cells which were prepared without defects. These small differences may not result in critical cell failures but could still affect overall cell capacity and performance. This additional information could be leveraged by correlating data from a large number of cell magnetic field maps with their synthesis/manufacturing conditions and electrochemical performance. It should be noted that the susceptibility measurements shown here can also be performed with cells that are not fully finished (i.e. do not contain electrolyte), and thus a manufacturer could potentially avoid a costly finishing and formation cycle of cells that are

shown to be defective at this stage. The defective cells studied here were in that form (without electrolyte) to illustrate this point.

[0080] Although many defects are clearly visible and interpretable from the field maps directly (Fig. 11), further opportunities arise when one considers a potentially high-throughput application. The measurements are sufficiently fast to be performed on a large number of cells, and the results could be correlated with additional cell characteristics to predict cell differences based on subtle features in the maps. To illustrate this point, a principal component analysis (PCA) was performed using the 2D images from Fig. 11 on the limited number of samples available. The PCA score plot is shown in Fig. 12, where a strong grouping can be seen for each of the cell types. Interestingly, while it could be difficult to visually differentiate between the non-defected cells and those with extra scraps, the PCA shows a clear grouping and separation using the second principal component.

[0081] In this example, the PCA was performed on the 2D magnetic field maps which are themselves reconstructed from multiple phase map images. In this kind of analysis there is no requirement for the input data to be a coherent image. Instead, optimized experiments could be designed that sample the regions of *k*-space that are expected to vary most strongly. In this manner, the diagnostic power of the experiments could be preserved (or even improved) while drastically reducing the overall experiment time. This latter approach could further benefit from a big data approach, in which machine learning algorithms could be used to more efficiently classify cells by defect type. In this way, one could further enhance the information content of the observed magnetic field maps.

[0082] Other Configurations

[0083] The above examples described an "inside-medium" setup (Case A of Fig. 5). In the "inside medium" setup, a container housing the conducting structure may be immersed in a detection medium. As used herein "immersed in a detection medium" may mean that the detection medium physically contacts the outer surface of the container or surrounds the outer surface of the container without physical contact. In another implementation, an "outside-

medium" setup is used in which the detection medium is placed in a vicinity of the battery (Case B of Fig. 5) at a predetermined distance (e.g., several centimeters or less), depending on the size of holder containing the battery, and the container containing the detection medium. In this implementation, the experimental protocol will be identical to that of the "inside-medium" setup described above, using the same MRI and image processing methodology to recover a field map of the detection medium, only the calculations used to fit the battery magnetic susceptibility will differ to reflect the geometry of the "outside-medium" setup. In the outside-medium setup, the holder only contains the battery. The holder does not contain detection medium. Instead, the detection medium is housed in a separate container. It is preferable that the container containing the detection medium is placed as close as possible to the holder containing the battery, but if there are strong magnetic artifacts, the detection medium can be moved further away to minimize the artifacts and maximize the useful signal. The preferred maximum distance between the detection medium and the battery is a few cm, but in some cases, the container containing the detection medium could be large (e.g., 10-30 cm diameter), thereby increasing the maximum distance. The maximum distance between the conducting structure and the detection medium is roughly equal to the battery dimensions. The detection medium for the "outside-medium" setup has the same minimal requirements described in the examples above. The radiofrequency coil can be placed immediately around the detection medium, or a bigger radiofrequency coil can used which encompasses the whole volume including the battery. The sensitivity will be better when the radiofrequency coil is placed immediately around the detection medium.

[0084] In a third implementation referred to as a "spectroscopic" setup (see Case C of Fig. 5), the idea of the "outside medium" setup is extended. In particular, the "spectroscopic" setup includes multiple detection volumes (i.e., the detection medium is divided into a plurality of separate volumes), each encapsulated in a radiofrequency coil with separate detection circuits. In this implementation, the detection medium is restricted to small volumes (< 1 cm^3), such that the field is uniform (<0.5 ppm variation) over the corresponding region. In this case, the measurement will consist of an NMR chemical shift spectrum (single pulse-acquire sequence) that will give a single estimate of ΔB_0 in the vicinity of each detection medium that are distributed in 3D around the battery. By fixing the coordinates of each detection medium with

respect to the battery position, $\Delta B_0(r)$, a finite region of the overall field map can be reconstructed and fit against a calculated susceptibility distribution in the same way as described for the imaged field maps. This method has the advantage of being much faster than the MRI-based techniques and can be performed without requiring MRI gradients.

[0085] Batteries are analyzed on the basis of changes in magnetic susceptibilities, a measure of the degree of magnetization of a material when a magnetic field is applied, and internal electric current distributions, which may change over the course of a charging/discharging cycle, and may be a result of battery degradation and failure. Either direct or alternating electrical current distributions can be measured. For the measurement of alternating current distributions, a pulse sequence can be used with pulse sequence elements, such as a radio-frequency pulse, which is modulated with the same frequency as the alternating electrical current. In this way, by analyzing phase-map images, one can obtain not only the magnitude of the current, but also the phase of the current. From this information, one can further obtain the localized distribution of impedances across the sample (i.e., the battery or the object of interest). The method can then be used to scan (in a localized way) the response of different parts of the object using different alternating electrical current frequencies. The inventors refer to this method as MR-based localized electrical impedance spectroscopy (MRLEIS).

[0086] The described susceptibility or electrical current measurements can be enhanced by (1) an inverse calculation of susceptibility maps or electrical current maps from the magnetic field maps using deconvolution or similar algorithms, and by (2) measuring magnetic field maps with the object oriented at different angles with respect to the static magnetic field. Both approaches can be combined. The orientation change is helpful for enhancing accuracy in the susceptibility or electrical current map calculations.

[0087] The properties leading to the observed magnetic field changes can be based on permanent or induced magnetic susceptibility, ferro-, para-, antiferro-, or diamagnetism, or electrical or ionic currents (direct or alternating current) within the object.

[0088] One particular embodiment may include electrochemical cells incorporated into a bigger device, such as a battery of several cells, or a cell or a battery incorporated into a device such as a cell phone, and the whole device could be analyzed in this fashion.

[0089] The systems and methods described in this specification use magnetic resonance to indirectly measure internal characteristics of a battery. By measuring the detection method, as opposed to the voltage and resistance/impedance of the battery itself, it is possible to evaluate the internal characteristics of any commercial battery of any geometry, including a commercial battery encased in conducting material. The method is fast and non-destructive. As discussed above, the lithiation state of cathodes, in particular, can be assessed at various stages in the charging cycle, although any overall susceptibility changes can be observed as well. Furthermore, it is possible to detect defects in cells, which could be determined even in unfinished cells (additional differences are observed between nominally non-defect cells). The methods described herein become particularly powerful if applied to large numbers of cells, where PCA or machine learning algorithms could operate on reduced data sets. Overall, the noninvasive methodology described herein enables faster progress in the development of new battery materials and cell designs that address current and future needs.

[0090] Implementations described in this specification can be implemented in digital electronic circuitry, or in computer software, firmware, or hardware, including the structures disclosed in this specification and their structural equivalents, or in combinations of one or more of them. The implementations described in this specification can be implemented as one or more computer programs, i.e., one or more modules of computer program instructions, encoded on one or more computer storage media for execution by, or to control the operation of, data processing apparatus. Alternatively or in addition, the program instructions can be encoded on an artificially-generated propagated signal, e.g., a machine-generated electrical, optical, or electromagnetic signal that is generated to encode information for transmission to suitable receiver apparatus for execution by a data processing apparatus. A computer storage medium can be, or be included in, a computer-readable storage device, a computer-readable storage substrate, a random or serial access memory array or device, or a combination of one or more of them. Moreover, while a computer storage medium is not a propagated signal, a computer storage

medium can be a source or destination of computer program instructions encoded in an artificially-generated propagated signal. The computer storage medium can also be, or be included in, one or more separate components or media (e.g., multiple CDs, disks, or other storage devices). Accordingly, the computer storage medium is both tangible and non-transitory.

[0091] As shown in Fig. 6, e.g., a computer-accessible medium 120 (e.g., as described herein, a storage device such as a hard disk, floppy disk, memory stick, CD-ROM, RAM, ROM, etc., or a collection thereof) can be provided (e.g., in communication with the processing arrangement 110). The computer-accessible medium 120 may be a non-transitory computer-accessible medium. The computer-accessible medium 120 can contain executable instructions 130 thereon. In addition or alternatively, a storage arrangement 140 can be provided separately from the computer-accessible medium 120, which can provide the instructions to the processing arrangement 110 so as to configure the processing arrangement to execute certain exemplary procedures, processes and methods, as described herein, for example. The instructions may include a plurality of sets of instructions. For example, in some implementations, the instructions may include instructions for applying radio frequency energy in a plurality of sequence blocks to a volume, where each of the sequence blocks includes at least a first stage. The instructions may further include instructions for repeating the first stage successively until magnetization at a beginning of each of the sequence blocks is stable, instructions for concatenating a plurality of imaging segments, which correspond to the plurality of sequence blocks, into a single continuous imaging segment, and instructions for encoding at least one relaxation parameter into the single continuous imaging segment.

[0092] System 100 may also include a display or output device, an input device such as a key-board, mouse, touch screen or other input device, and may be connected to additional systems via a logical network. Many of the embodiments described herein may be practiced in a networked environment using logical connections to one or more remote computers having processors. Logical connections may include a local area network (LAN) and a wide area network (WAN) that are presented here by way of example and not limitation. Such networking environments are commonplace in office-wide or enterprise-wide computer networks, intranets

and the Internet and may use a wide variety of different communication protocols. Those skilled in the art can appreciate that such network computing environments can typically encompass many types of computer system configurations, including personal computers, hand-held devices, multi-processor systems, microprocessor-based or programmable consumer electronics, network PCs, minicomputers, mainframe computers, and the like. Embodiments of the invention may also be practiced in distributed computing environments where tasks are performed by local and remote processing devices that are linked (either by hardwired links, wireless links, or by a combination of hardwired or wireless links) through a communications network. In a distributed computing environment, program modules may be located in both local and remote memory storage devices.

[0093] Various embodiments are described in the general context of method steps, which may be implemented in one embodiment by a program product including computer-executable instructions, such as program code, executed by computers in networked environments. Generally, program modules include routines, programs, objects, components, data structures, etc. that perform particular tasks or implement particular abstract data types. Computer-executable instructions, associated data structures, and program modules represent examples of program code for executing steps of the methods disclosed herein. The particular sequence of such executable instructions or associated data structures represents examples of corresponding acts for implementing the functions described in such steps.

[0094] Software and web implementations of the present invention could be accomplished with standard programming techniques with rule based logic and other logic to accomplish the various database searching steps, correlation steps, comparison steps and decision steps. It should also be noted that the words "component" and "module," as used herein and in the claims, are intended to encompass implementations using one or more lines of software code, and/or hardware implementations, and/or equipment for receiving manual inputs.

[0095] With respect to the use of substantially any plural and/or singular terms herein, those having skill in the art can translate from the plural to the singular and/or from the singular to the plural as is appropriate to the context and/or application. The various singular/plural

permutations may be expressly set forth herein for the sake of clarity. In some cases, the actions recited in the claims can be performed in a different order and still achieve desirable results. In addition, the processes depicted in the accompanying figures do not necessarily require the particular order shown, or sequential order, to achieve desirable results. In certain implementations, multitasking and parallel processing may be advantageous. Thus, particular implementations of the invention have been described.

[0096] The foregoing description of illustrative embodiments has been presented for purposes of illustration and of description. It is not intended to be exhaustive or limiting with respect to the precise form disclosed, and modifications and variations are possible in light of the above teachings or may be acquired from practice of the disclosed embodiments. Therefore, the above embodiments should not be taken as limiting the scope of the invention.

WHAT IS CLAIMED:

1. A method of diagnosing a conducting structure, the method comprising:

providing the conducting structure in a magnetic field;

performing one of:

immersing a container housing the conducting structure in a detection medium, or

providing the detection medium at a predetermined distance from the conducting structure;

exciting nuclear or electronic spins within the detection medium using an electromagnetic signal having a first frequency;

receiving an electromagnetic signal having a second frequency from the detection medium;

obtaining a frequency distribution of the detection medium; and

indirectly measuring internal characteristics of the conducting structure by characterizing frequency changes in the frequency distribution.

2. The method of claim 1, wherein the conducting structure is a battery, a capacitor, a supercapacitor, or a fuel cell.

3. The method of any of the preceding claims, wherein the measurements are performed either during charging or discharging, either while current is flowing, or while current is stopped.

4. The method of any of the preceding claims, wherein the internal characteristics of the conducting structure are modeled on the basis of magnetic susceptibility differences and changes within the conducting structure.

5. The method of claim 4, wherein modeling on the basis of magnetic susceptibility differences and changes within the conducting structure comprises:

assigning one or more regions within the conducting structure a given magnetic susceptibility; and

calculating a generated magnetic field based on an effect on the detection medium,

wherein susceptibilities of the one or more regions form parameters configured to be fit by minimizing differences between a calculated frequency distribution and a measured frequency distribution in the detection medium.

6. The method of any of claims 1-4, wherein the internal characteristics of the conducting structure are modeled on the basis of current distributions within the conducting structure.

7. The method of claim 6, wherein modeling on the basis of current distributions within the conducting structure comprises:

assigning one or more regions within the conducting structure a given current distribution; and

calculating a generated magnetic field based on an effect on the detection medium,

wherein amplitudes of current distributions of the one or more regions form parameters configured to be fit by minimizing differences between a calculated frequency distribution and a measured frequency distribution in the detection medium.

8. The method of any one of claims 1-4, wherein

the internal characteristic measured is a state of charge of the conducting structure, and

the state of charge of the conducting structure is measured by converting the frequency distribution of the detection medium into a state of charge.

10. The method of claim 1, wherein the conducting structure is a catalyst material.

11. The method of any of the preceding claims, wherein the method comprises immersing the container housing the conducting structure in the detection medium.

12. The method of any of the preceding claims, wherein the method comprises providing the detection medium at a predetermined distance from the conducting structure.

13. The method of any of the preceding claims, wherein the detection medium comprises water or water doped with a paramagnetic species.

14. A system for diagnosing internal characteristics of a conducting structure, the system comprising:

an NMR/MRI magnet;

at least one radiofrequency coil removably positioned within the NMR/MRI magnet;

a holder configured to receive a conducting structure; and

a detection medium,

wherein internal characteristics of the conducting structure are indirectly measured by exciting nuclear or electronic spins within the detection medium using a first electromagnetic signal having a first frequency, receiving a second electromagnetic signal having a second frequency from the detection medium. obtaining a frequency distribution of the detection medium, and characterizing frequency changes in the frequency distribution.

15. The system of claim 14, wherein the holder comprises

a first detection medium chamber configured to receive a volume of the detection medium;

a second detection medium chamber configured to receive a volume of the detection medium, and

a conducting structure chamber provided between the first detection medium chamber and the second detection medium chamber, and configured to receive the conducting structure.

16. The system of claim 14, wherein the detection medium is provided at a predetermined distance from the conducting structure.

17. The system of claim 14 or claim 16, further comprising:

a plurality of containers arranged around the holder and a predetermined distance from the holder, each container housing a volume of a detection medium.

18. The system of any one of claims 14-17, wherein the conducting structure comprises a battery, a capacitor, a supercapacitor, a fuel cell, or a catalyst material.

19. The system of any one of claims 14-18, wherein the detection medium comprises water or water doped with a paramagnetic species.

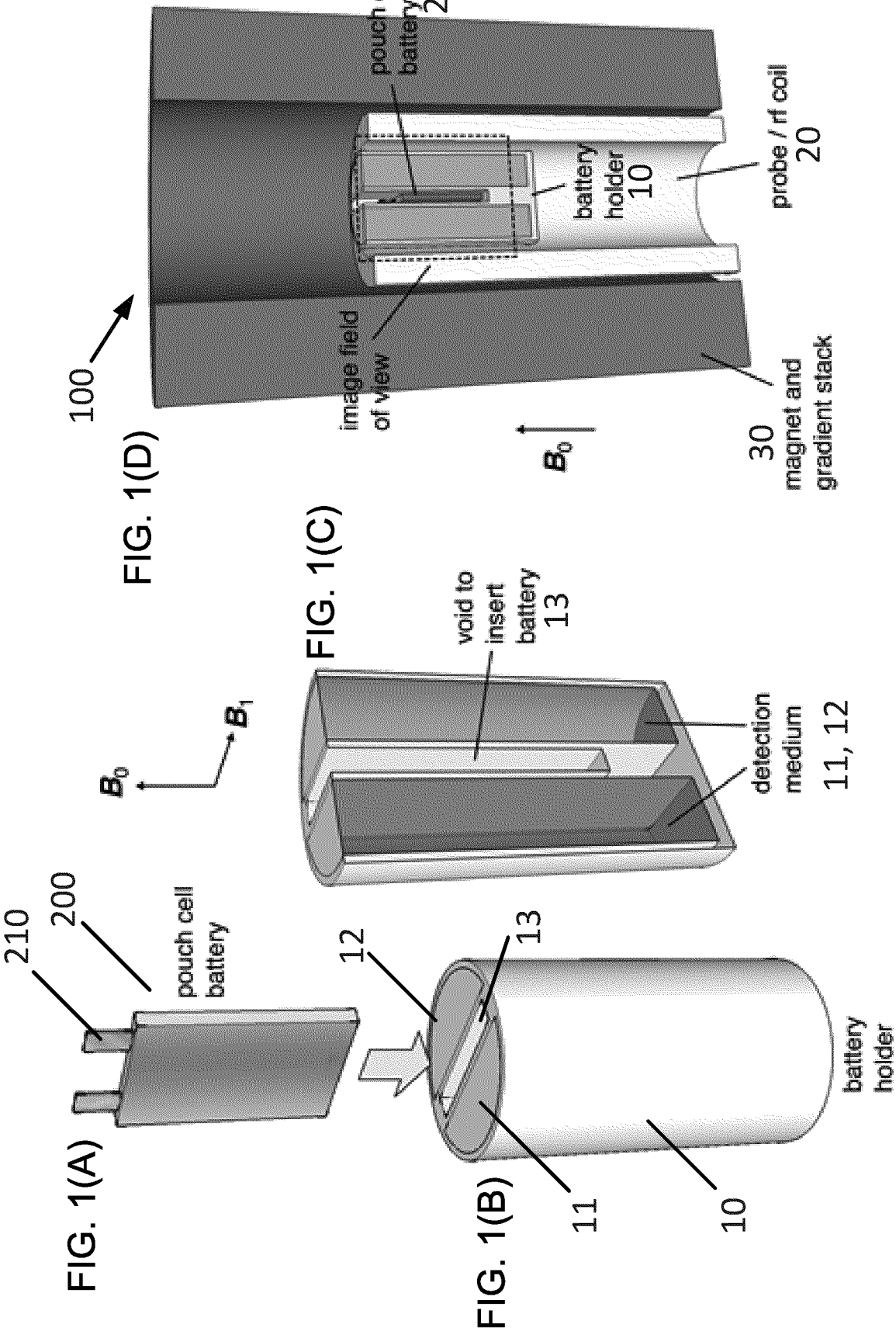


FIG. 1(A)

FIG. 1(B)

FIG. 1(C)

FIG. 1(D)

FIG. 1(E)

RIT cell

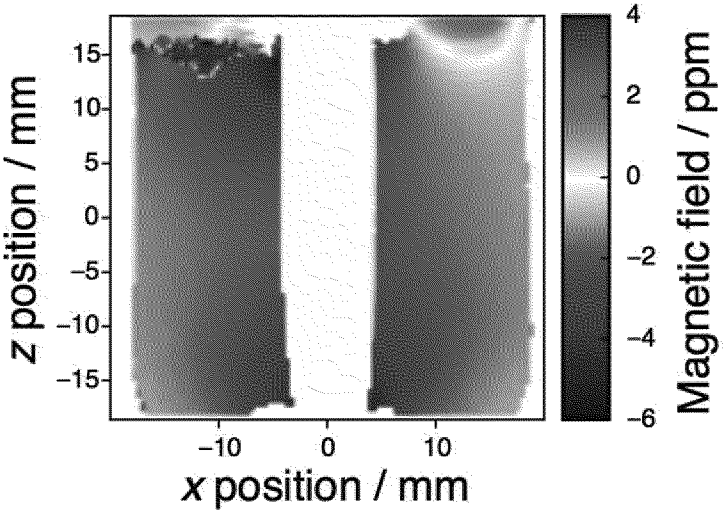
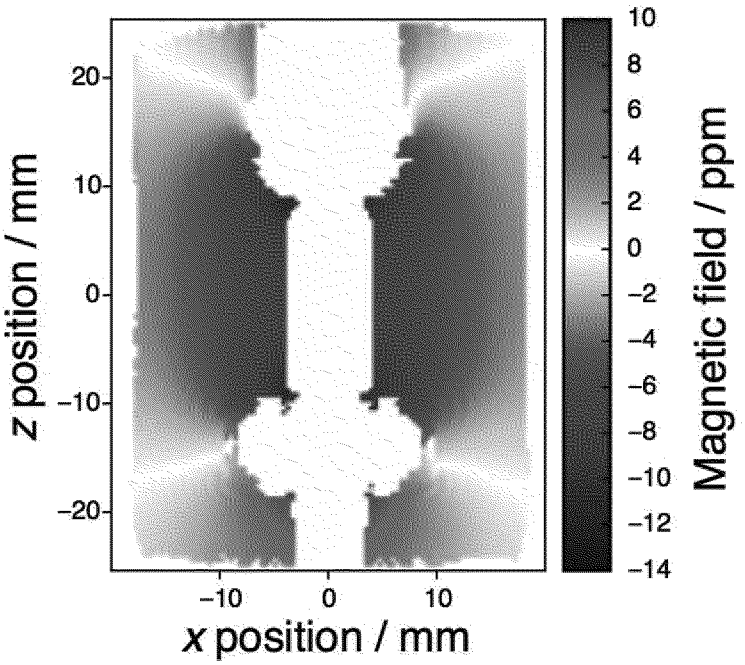


FIG. 1(F)

Commercial cell



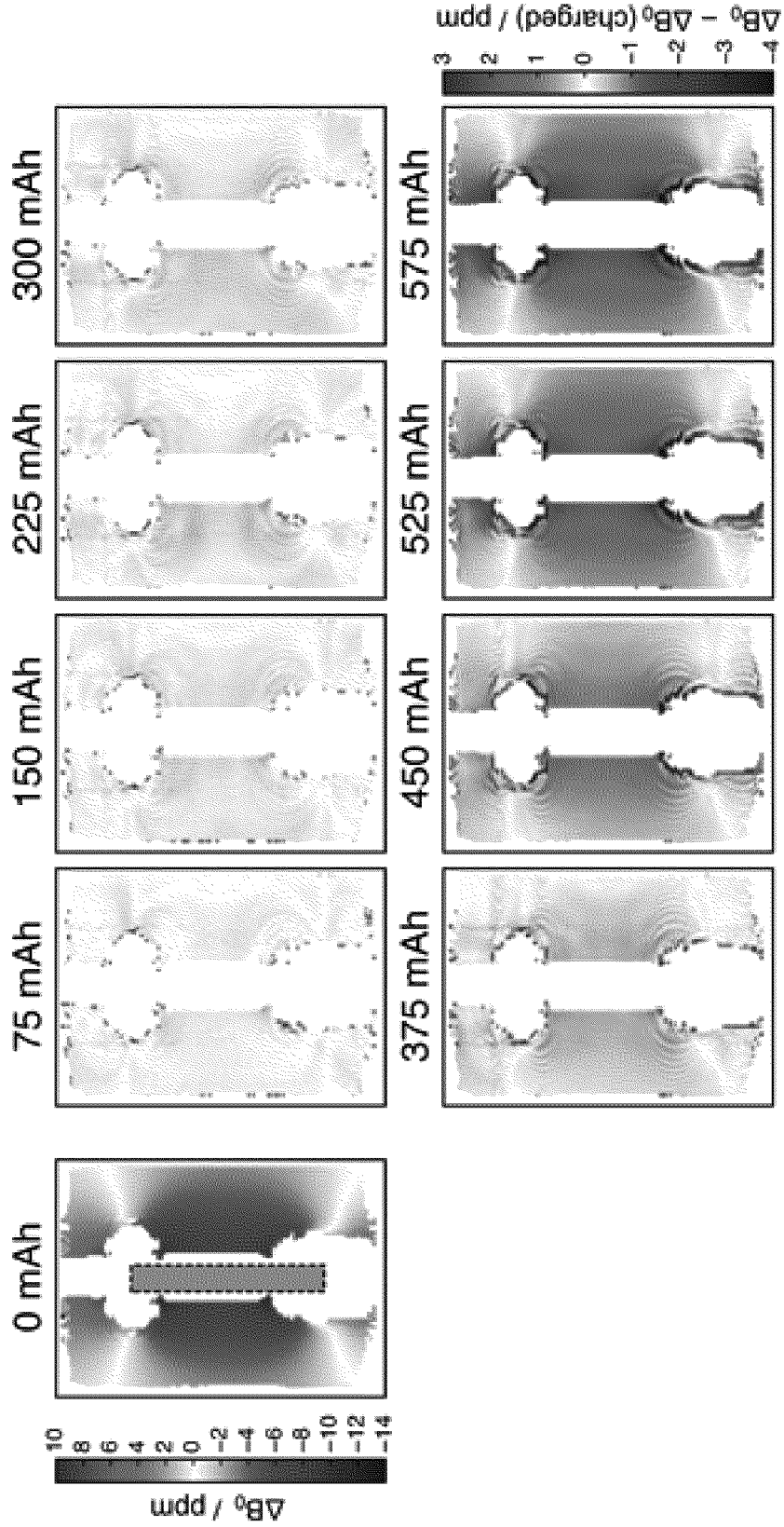

0 mAh
75 mAh
150 mAh
225 mAh
300 mAh
375 mAh
450 mAh
525 mAh
575 mAh
ΔB0 / ppm
10 8 6 4 2 0 -2 -4 -6 -8 -10 -12 -14
ΔB0 – ΔB0 (charged) / ppm
3 2 1 0 -1 -2 -3 -4

FIG. 2

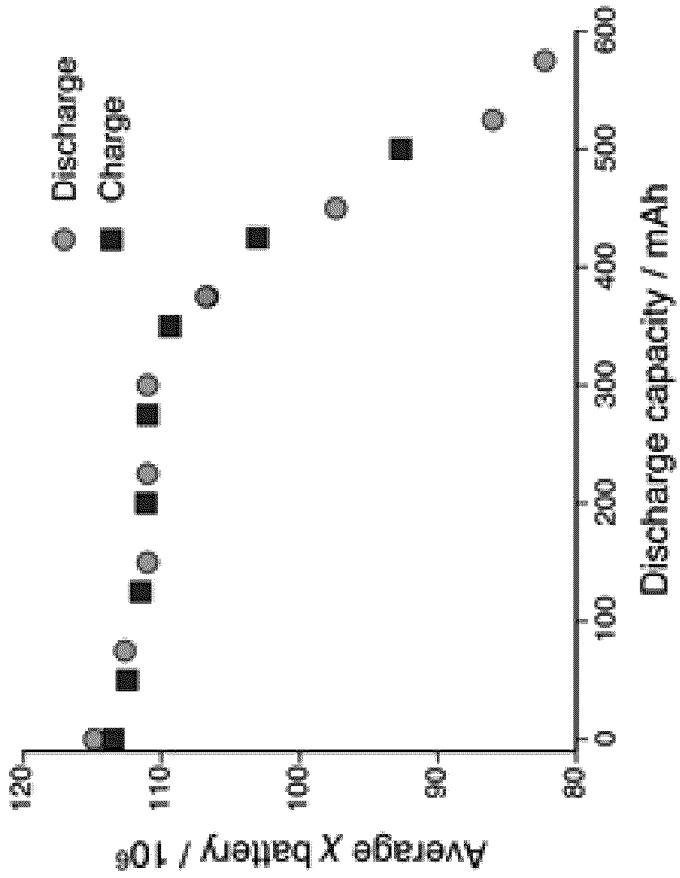

Discharge
Charge
Average X battery / 10^6
120
110
100
90
80
0
100
200
300
400
500
600
Discharge capacity / mAh

FIG. 3

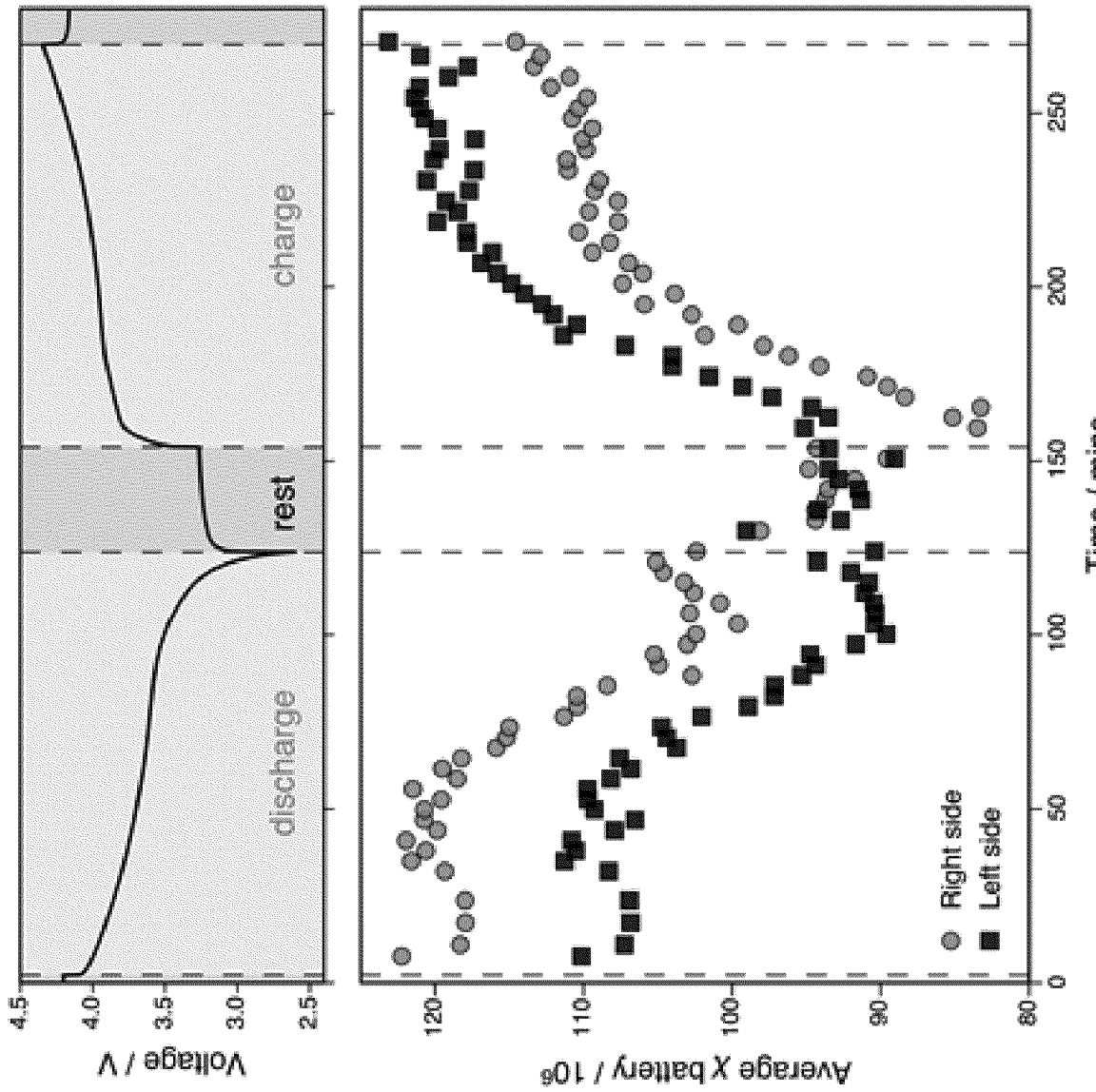

Voltage / V
4.5
4.0
3.5
3.0
2.5
discharge
rest
charge
Average X battery / 10^6
120
110
100
90
80
Right side
Left side
0
50
100
150
200
250
Time / mins

FIG. 4

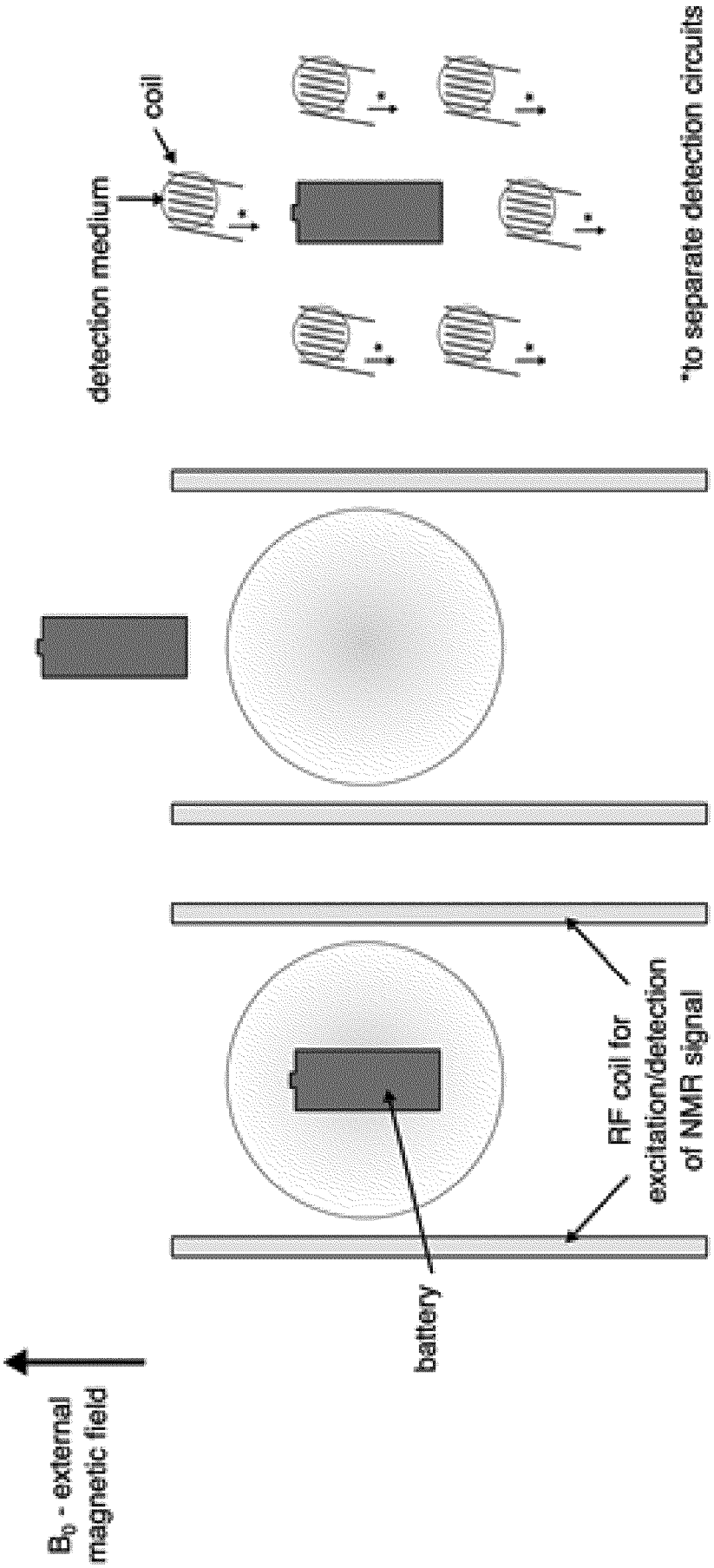

Case A: Battery surrounded by detection medium
Case B: Battery outside of detection medium
Case C: Battery outside of uniform detection medium
coil
detection medium
*to separate detection circuits
B_0 - external magnetic field
battery
RF coil for excitation/detection of NMR signal

FIG. 5

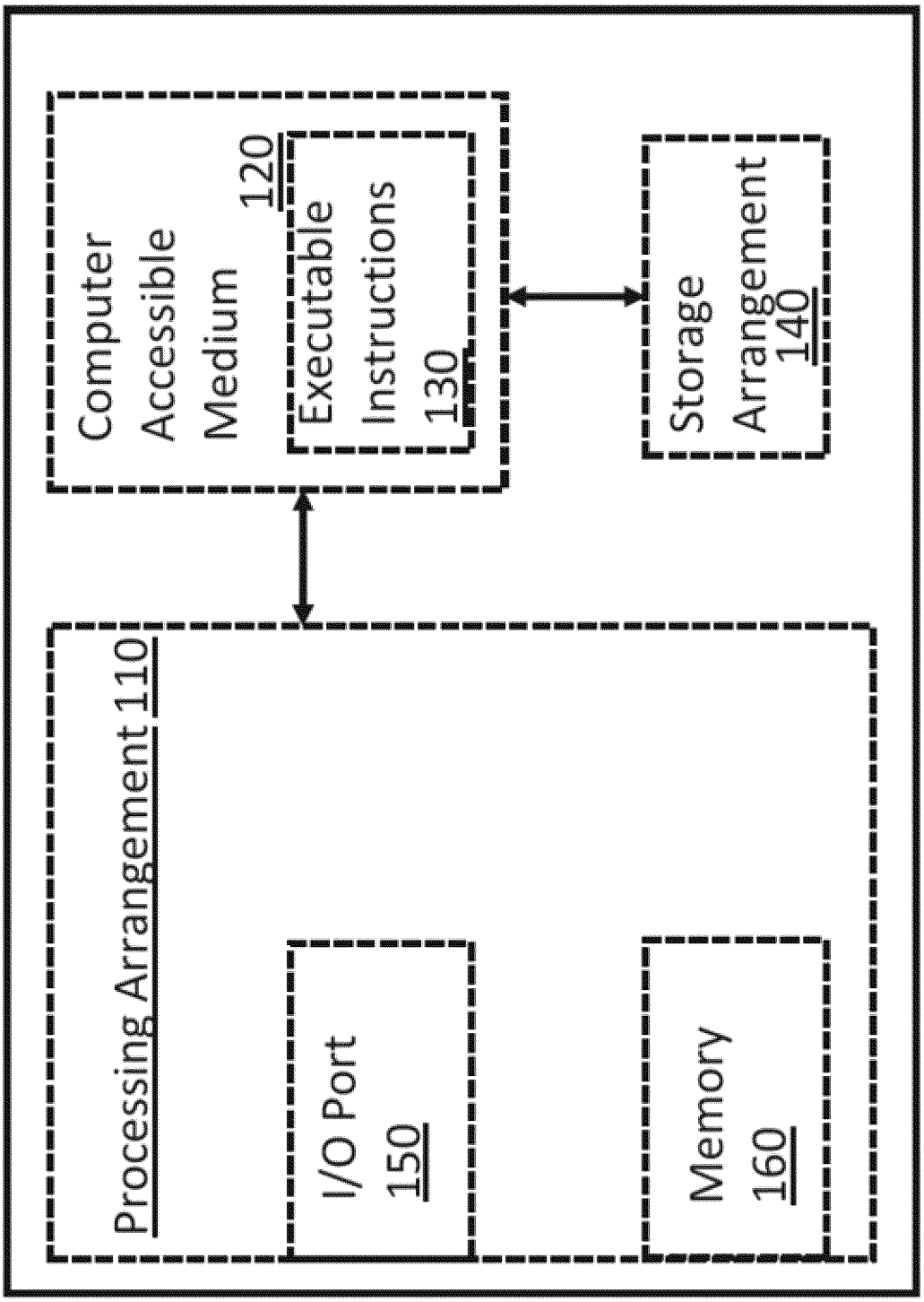

Computer Accessible Medium 120
Executable Instructions 130
Storage Arrangement 140
Processing Arrangement 110
I/O Port 150
Memory 160

FIG. 6

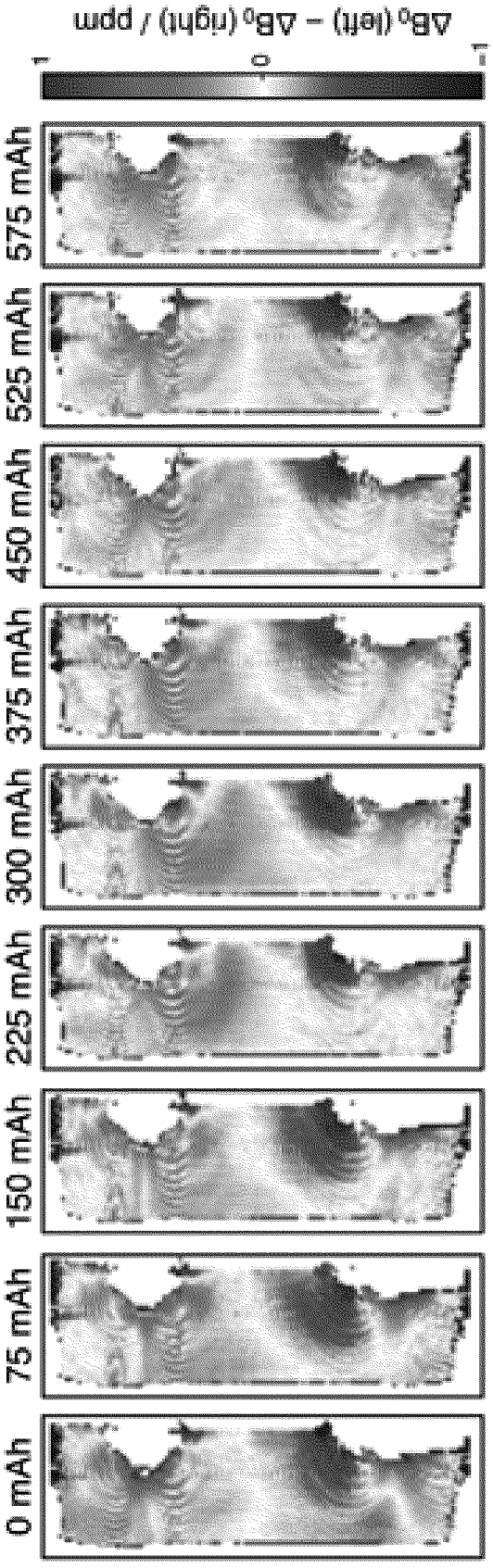

ΔB0 (left) – ΔB0 (right) / ppm
1
0
-1
0 mAh
75 mAh
150 mAh
225 mAh
300 mAh
375 mAh
450 mAh
525 mAh
575 mAh

FIG. 7

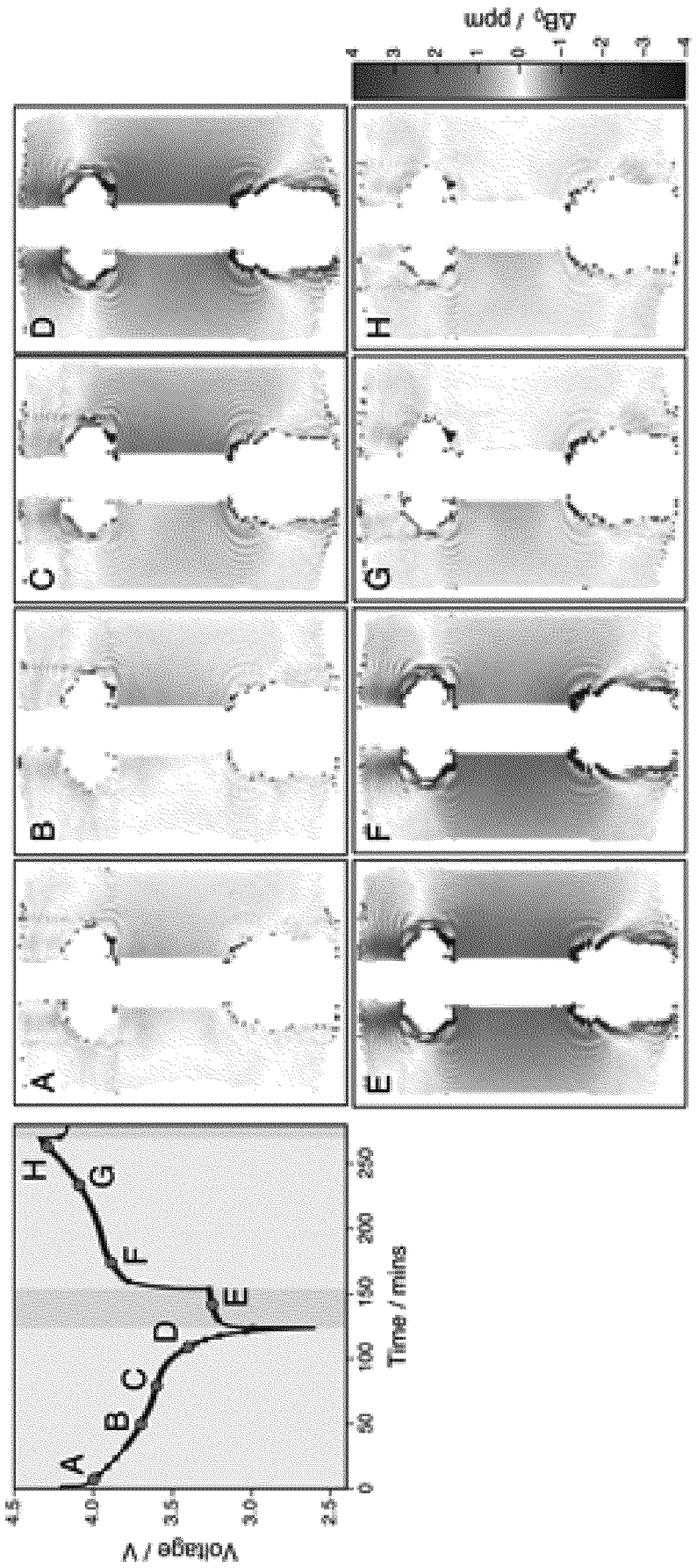


FIG. 8

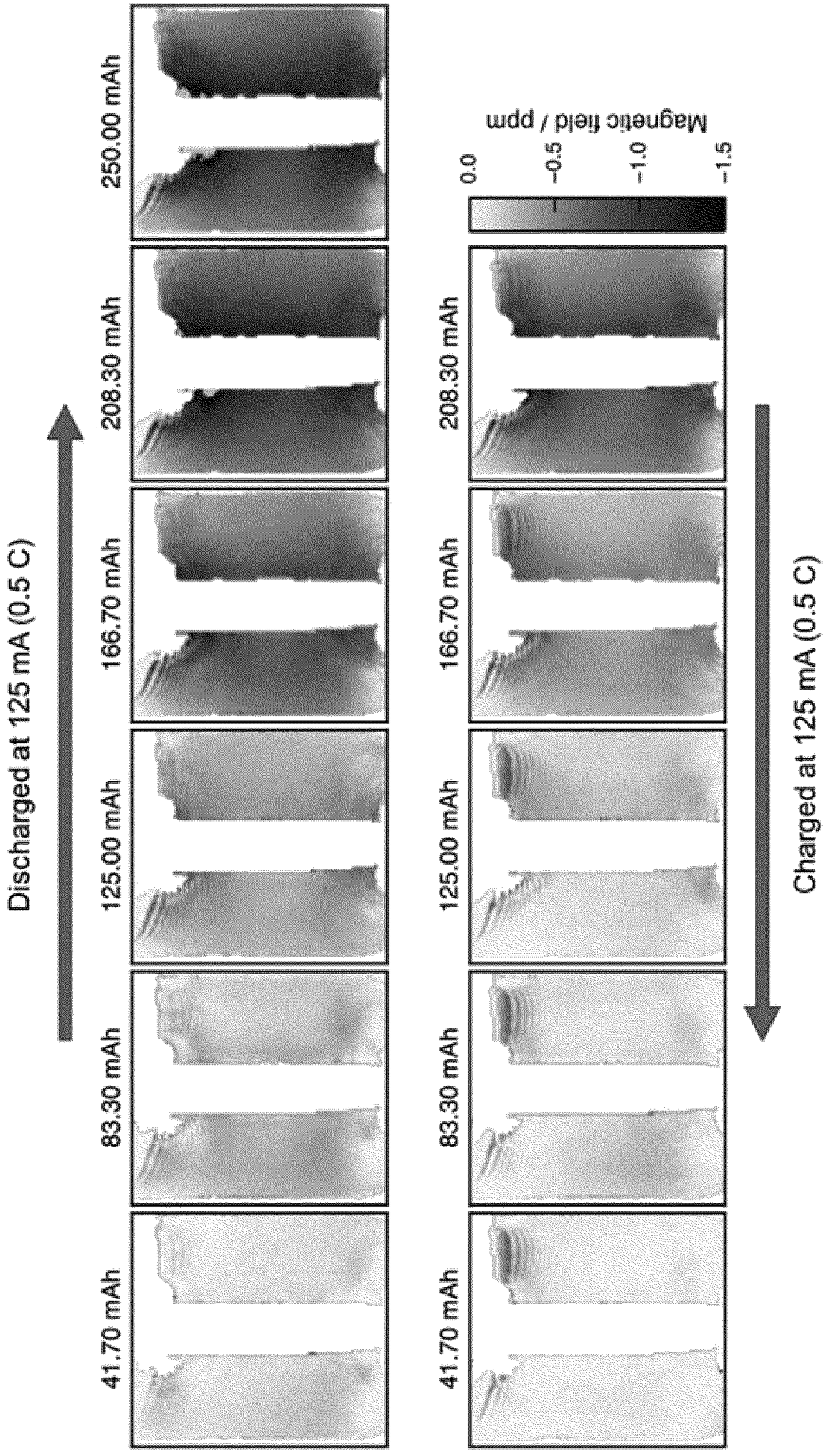

Discharged at 125 mA (0.5 C)
250.00 mAh
208.30 mAh
166.70 mAh
125.00 mAh
83.30 mAh
41.70 mAh
Magnetic field / ppm
0.0
−0.5
−1.0
−1.5
208.30 mAh
166.70 mAh
125.00 mAh
83.30 mAh
41.70 mAh
Charged at 125 mA (0.5 C)

FIG. 9

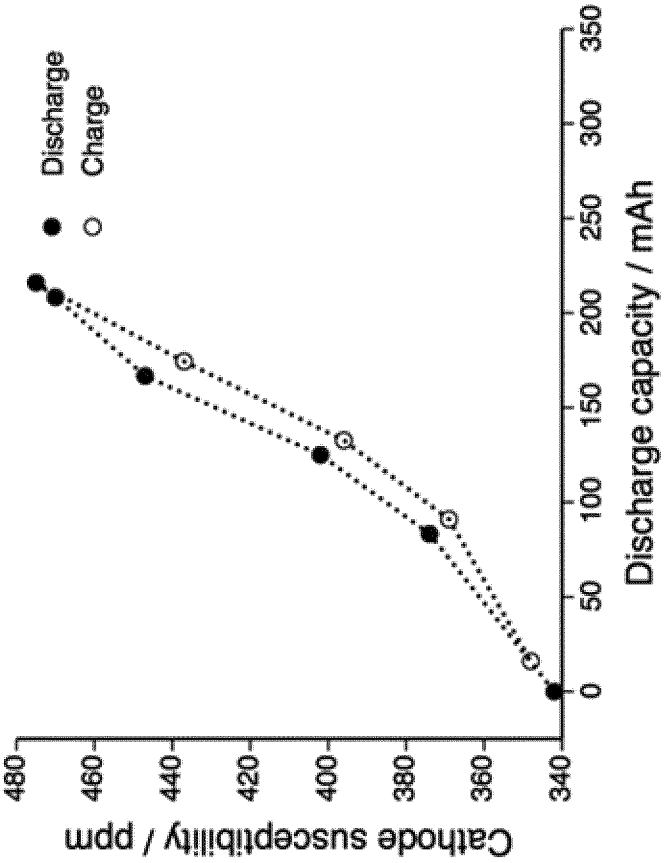


FIG. 10(B)

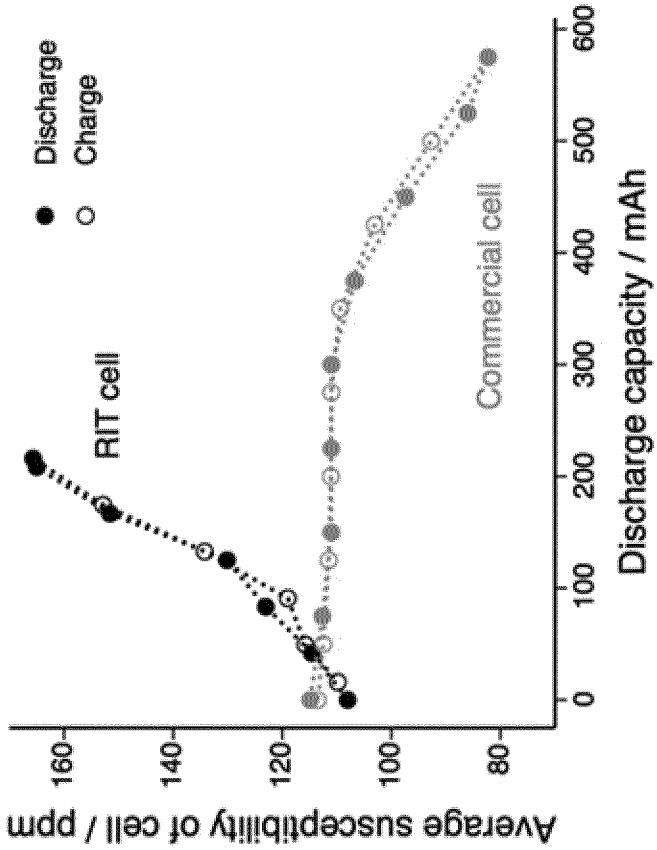


FIG. 10(A)

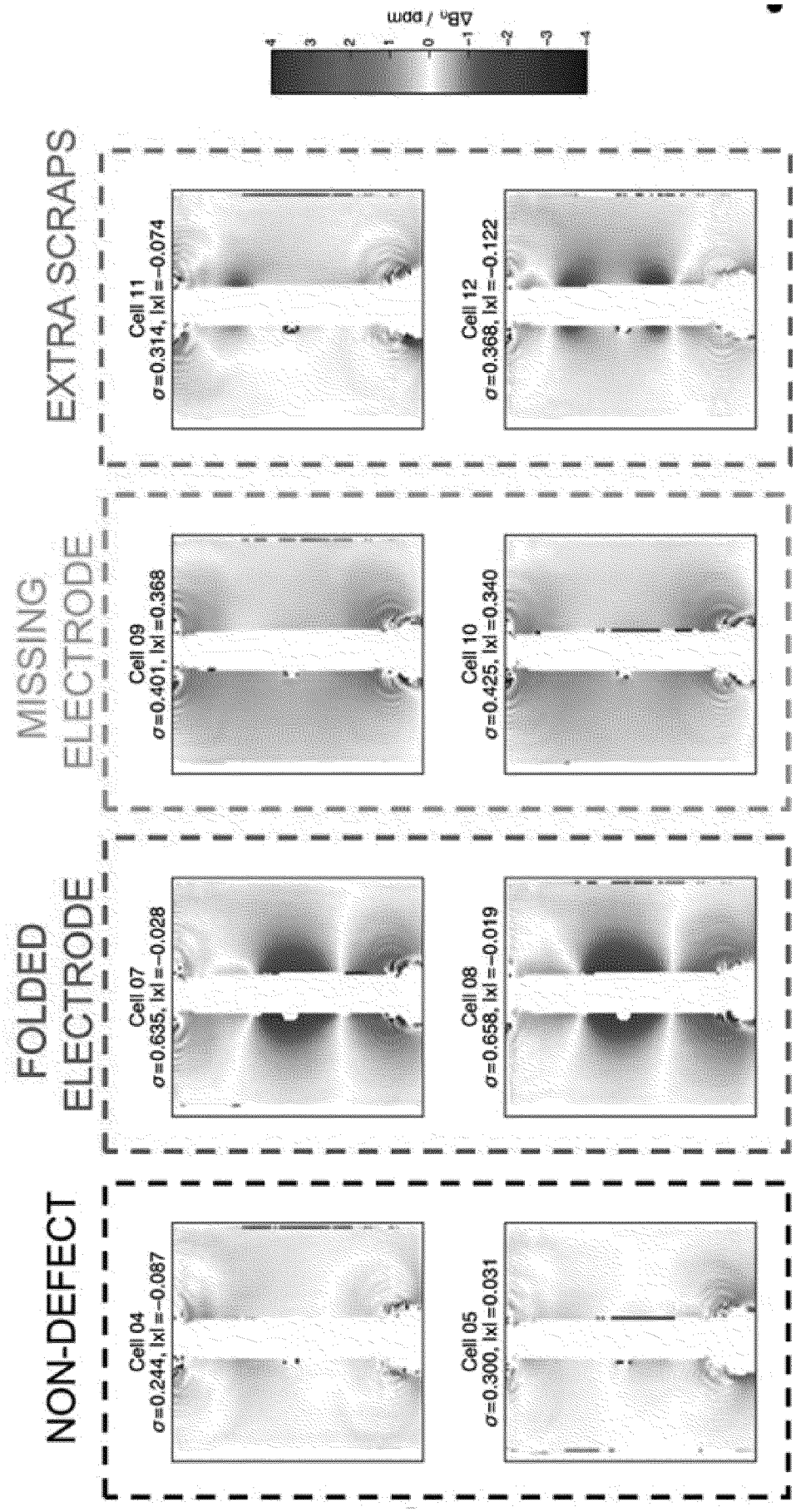

NON-DEFECT
FOLDED ELECTRODE
MISSING ELECTRODE
EXTRA SCRAPS
Cell 04
σ=0.244, Ixl =−0.087
Cell 05
σ=0.300, Ixl =0.031
Cell 07
σ=0.635, Ixl =−0.028
Cell 08
σ=0.658, Ixl =−0.019
Cell 09
σ=0.401, Ixl =0.368
Cell 10
σ=0.425, Ixl =0.340
Cell 11
σ=0.314, Ixl =−0.074
Cell 12
σ=0.368, Ixl =−0.122
ΔBn / ppm
4
3
2
1
0
-1
-2
-3
-4

FIG. 11

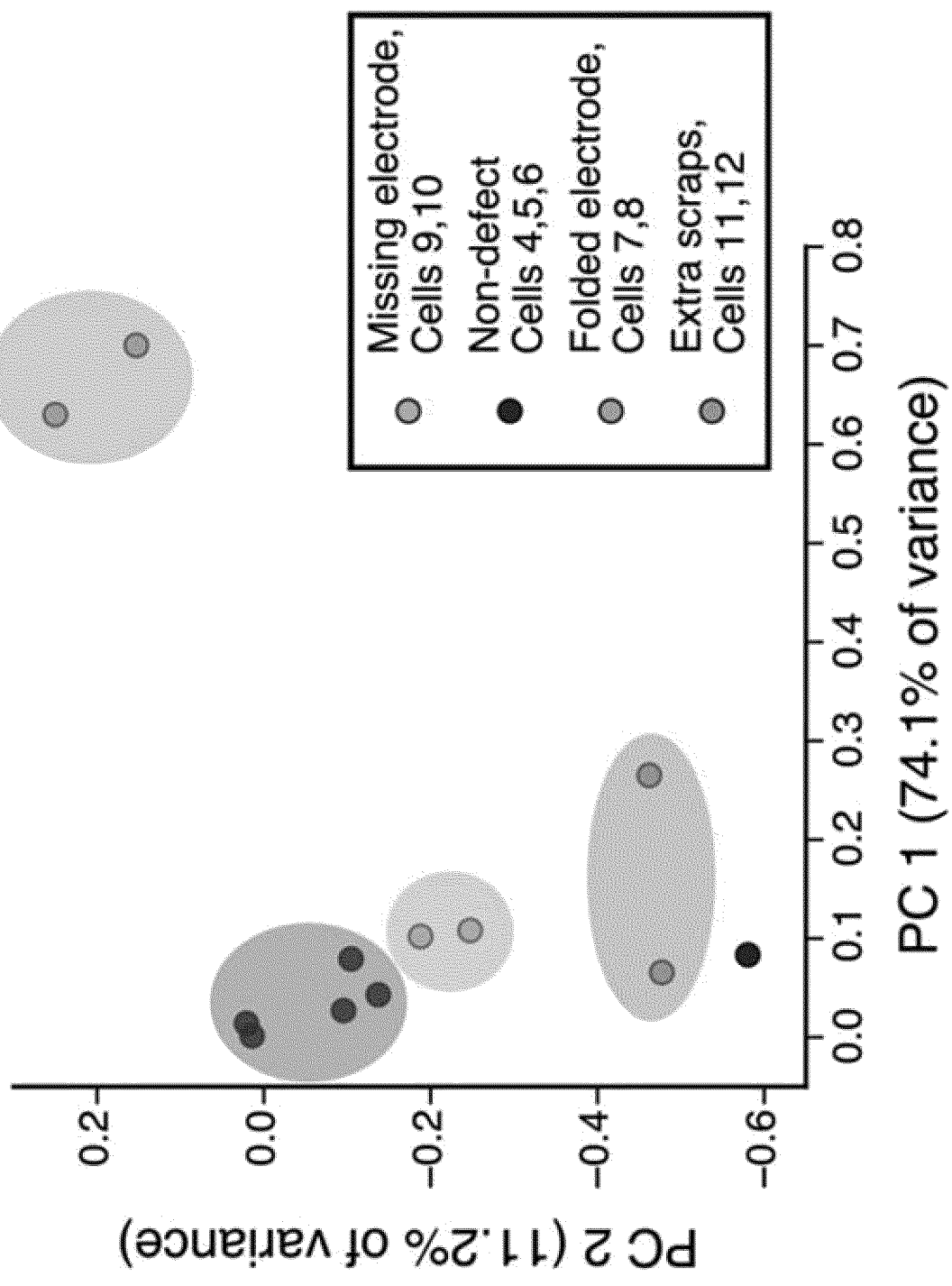

Missing electrode, Cells 9,10
Non-defect Cells 4,5,6
Folded electrode, Cells 7,8
Extra scraps, Cells 11,12
PC 2 (11.2% of variance)
PC 1 (74.1% of variance)
0.2
0.0
−0.2
−0.4
−0.6
0.0
0.1
0.2
0.3
0.4
0.5
0.6
0.7
0.8

FIG. 12

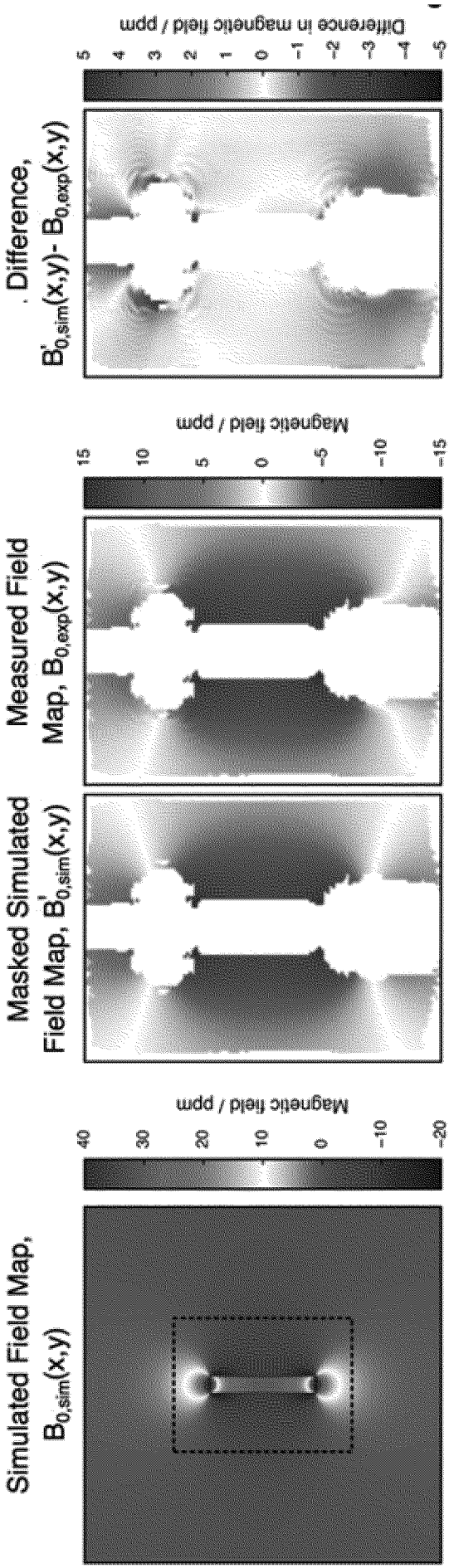

Simulated Field Map, $B_{0,sim}(x,y)$
Magnetic field / ppm
40
30
20
10
0
−10
−20
Masked Simulated Field Map, $B'_{0,sim}(x,y)$
Measured Field Map, $B_{0,exp}(x,y)$
Magnetic field / ppm
15
10
5
0
−5
−10
−15
Difference, $B'_{0,sim}(x,y) - B_{0,exp}(x,y)$
Difference in magnetic field / ppm
5
4
3
2
1
0
−1
−2
−3
−4
−5

FIG. 13

INTERNATIONAL SEARCH REPORT

International application No.
PCT/US 17/64948

Box No. II Observations where certain claims were found unsearchable (Continuation of item 2 of first sheet)

This international search report has not been established in respect of certain claims under Article 17(2)(a) for the following reasons:

1. ☐ Claims Nos.:
because they relate to subject matter not required to be searched by this Authority, namely:

2. ☐ Claims Nos.:
because they relate to parts of the international application that do not comply with the prescribed requirements to such an extent that no meaningful international search can be carried out, specifically:

3. ☒ Claims Nos.: 4-8, 11-13, 18, 19
because they are dependent claims and are not drafted in accordance with the second and third sentences of Rule 6.4(a).

Box No. III Observations where unity of invention is lacking (Continuation of item 3 of first sheet)

This International Searching Authority found multiple inventions in this international application, as follows:

1. ☐ As all required additional search fees were timely paid by the applicant, this international search report covers all searchable claims.

2. ☐ As all searchable claims could be searched without effort justifying additional fees, this Authority did not invite payment of additional fees.

3. ☐ As only some of the required additional search fees were timely paid by the applicant, this international search report covers only those claims for which fees were paid, specifically claims Nos.:

4. ☐ No required additional search fees were timely paid by the applicant. Consequently, this international search report is restricted to the invention first mentioned in the claims; it is covered by claims Nos.:

Remark on Protest

☐ The additional search fees were accompanied by the applicant's protest and, where applicable, the payment of a protest fee.

☐ The additional search fees were accompanied by the applicant's protest but the applicable protest fee was not paid within the time limit specified in the invitation.

☐ No protest accompanied the payment of additional search fees.

INTERNATIONAL SEARCH REPORT

International application No.
PCT/US 17/64948

A. CLASSIFICATION OF SUBJECT MATTER
IPC(8) - G01R 33/44, G01N 23/00, G01N 15/08, G01N 24/00 (2018.01)
CPC - Y10T 436/24, G01R 33/44, G01R 33/46, G01N 24/08, G01N 15/08

According to International Patent Classification (IPC) or to both national classification and IPC

B. FIELDS SEARCHED

Minimum documentation searched (classification system followed by classification symbols)
See Search History Document

Documentation searched other than minimum documentation to the extent that such documents are included in the fields searched
See Search History Document

Electronic data base consulted during the international search (name of data base and, where practicable, search terms used)
See Search History Document

C. DOCUMENTS CONSIDERED TO BE RELEVANT

Category*	Citation of document, with indication, where appropriate, of the relevant passages	Relevant to claim No.
Y --- A	US 2007/0287184 A1 (TELKKI et al.) 13 December 2007 (13.12 2007), Fig 7; para [0001], [0003], [0018], [0021]-[0023], [0043], [0044], [0081], [0088], [0090]	1-3, 10, 14, 16 --- 15, 17
Y --- A	US 2016/0116540 A1 (FLORIDA STATE UNIVERSITY RESEARCH FOUNDATION) 28 April 2016 (28.04.2016), para [0003], [0014], [0018], [0062], [0068]-[0074], [0081]	1-3, 10, 14, 16 --- 15, 17
Y	US 2014/0184224 A1 (NEVO et al.) 03 July 2014 (03.07.2014), para [0004], [0013], [0018], [0101]	10
A	US 6,774,635 B1 (GERALD, II et al.) 10 August 2004 (10.08.2004), entire document	1-3, 10, 14-17

☐ Further documents are listed in the continuation of Box C. ☐ See patent family annex.

* Special categories of cited documents:
"A" document defining the general state of the art which is not considered to be of particular relevance
"E" earlier application or patent but published on or after the international filing date
"L" document which may throw doubts on priority claim(s) or which is cited to establish the publication date of another citation or other special reason (as specified)
"O" document referring to an oral disclosure, use, exhibition or other means
"P" document published prior to the international filing date but later than the priority date claimed
"T" later document published after the international filing date or priority date and not in conflict with the application but cited to understand the principle or theory underlying the invention
"X" document of particular relevance; the claimed invention cannot be considered novel or cannot be considered to involve an inventive step when the document is taken alone
"Y" document of particular relevance; the claimed invention cannot be considered to involve an inventive step when the document is combined with one or more other such documents, such combination being obvious to a person skilled in the art
"&" document member of the same patent family

Date of the actual completion of the international search	Date of mailing of the international search report
05 February 2018	28 FEB 2018
Name and mailing address of the ISA/US Mail Stop PCT, Attn: ISA/US, Commissioner for Patents P.O. Box 1450, Alexandria, Virginia 22313-1450 Facsimile No. 571-273-8300	Authorized officer: Lee W. Young PCT Helpdesk: 571-272-4300 PCT OSP: 571-272-7774